Nonlinear Dyn (2024) 112:7909–7949
https://doi.org/10.1007/s11071-024-09520-z

ORIGINAL PAPER

Dynamic characteristics and experimental verification of planetary gear-motor coupling system under unsteady and non-ideal states

Kongliang Zhang · Hongkun Li · Shunxin Cao · Chen Yang · Wei Xiang

Received: 5 December 2023 / Accepted: 11 March 2024 / Published online: 25 March 2024

Abstract As the integral component of various high-end equipment, the dynamic characteristics of planetary gear-motor coupling system (PMCS) is susceptible to the influence of electrical or mechanical subsystems. Especially under complex non-steady state and non-ideal scenarios, the coupling mechanisms between the gear transmission system and the electrical system remain unclear. To address the challenging issue, this study comprehensively takes into account both the internal and external excitations of the mechanical transmission system, and established a planetary gear dynamic model that applicable to analyze the dynamic response under various unsteady conditions; Simultaneously, this study introduces the Rotor Flux Orientation Control (RFOC) algorithm, the Space Vector Pulse Width Modulation (SVPWM), as well as the three-phase asynchronous motor equivalent circuit model and inverter power supply model. Then established the comprehensive drive chain coupling model by combining with the former planetary gear models. The correctness of the model is verified by the simulation and experimental results of the PMCS under steady-state conditions. Thereafter, this study uncovers the vibration-current coupling mechanisms of the gear-motor system in non-steady-state conditions. Furthermore, the dynamic characteristics of the PMCS in non-ideal scenarios are investigated. This work also provides theoretical guidance for condition monitoring of the whole electromechanical systems.

Keywords Planetary gearbox · Electromechanical coupling system · Unsteady state conditions · Non-ideal state · Dynamic response

K. Zhang · H. Li (✉) · S. Cao · C. Yang · W. Xiang
School of Mechanical Engineering, Dalian University of Technology, Dalian 116024, China
e-mail: lihk@dlut.edu.cn

K. Zhang · H. Li · S. Cao · C. Yang · W. Xiang
State Key Laboratory of High-Performance Precision Manufacturing, Dalian University of Technology, Dalian 116024, China

1 Introduction

The electromechanical coupling system (EMCS) serves as a critical component in major equipment such as wind turbines, new energy vehicles, port equipment, and CNC machine tools [1, 2]. When operating in harsh environments with complex and variable conditions, the cyclic changes in rotational speeds and loads can lead to the deterioration of gear meshing conditions. This deterioration, in turn, reduces the reliability of the equipment. The dynamics of EMCS become increasingly complex. As the most representative EMCS in large-scale equipment, it is of paramount importance to establish a refined dynamic model of electromechanical coupling that accounts for various influencing factors. This model aims to

comprehensively analyze the stability and dynamics of the motor-gear coupling system under the complex and variable working conditions. The ultimate goal is to enhance the overall reliability of the system.

Existing research on EMCSs primarily focuses on two key aspects: gear dynamics and monitoring/diagnosis of motor stator currents. In the field of gear dynamics modeling, several notable contributions have been made: Kahraman [3] considered several manufacturing errors and assembly variations, established a nonlinear dynamics model of the planetary drive system, and investigated the load sharing characteristics of the planetary drive system. Parker et al. [4] considered different coordinate systems, made corrections based on the Kahraman's model, and investigated the natural frequency spectra and vibration modes of planetary gears. Guo et al. [5] developed a planetary gearbox dynamics model based on the lumped parameter method by considering tooth separation, back-side contact, tooth wedging, and bearing clearances based on Parker. In a certain speed range, the nonlinear wedging behavior of the gear teeth causes a very obvious impact on the bearing force. Kim et al. [6] consider the effect of gear vibration on the pressure angle and overlap of gears during operation. Subsequent studies in dynamic modeling of planetary drive systems have extended the above-mentioned models. They consider additional factors such as oil film stiffness [7, 8], ring gear flexibility [9, 10], bearing misalignment [11], and gear failures [12–15], resulting in more detailed and comprehensive dynamic models. In the context of establishing gear dynamic models, numerous scholars have developed mature theories and provided numerous modeling and analysis cases, whether employing lumped parameter methods, finite element analysis, or rigid-flexible coupling methods. These developments have laid a theoretical foundation for the mechanical dynamics modeling of the motor-gear EMCS. However, the literature mentioned above tends to place substantial constraints on the consideration of the driving part of the gear transmission system. It commonly simplifies it as a constant or fluctuating torque without accounting for the influences of electrical and motor systems. Furthermore, these studies have not delved into the coupling mechanisms of the motor-gear system, particularly overlooking the exploration of coupling effects from the perspective of motor current characteristics.

Traditional methods of monitoring mechanical equipment using vibration signals face challenges such as noise interference, complex transmission paths, and difficulties in sensor installation. Fortunately, monitoring the status of drive systems using motor current can address these issues effectively. Motor Current Signature Analysis (MCSA) is a robust method for monitoring motors and mechanical equipment, and this method is an interference-resistant method. In the field of MCSA, Feki et al. [16]have utilized the *d-q* vector method to detect gear tooth damage-related characteristics in current signals, investigating the sensitivity of current signals to different positions and shapes of tooth damage. Ottewill et al. [17] applied a time-domain synchronous averaging algorithm to gear-motor system condition monitoring, confirming the effectiveness of this method for current signal analysis through simulations and experiments. Feng et al. [18] developed an AM-FM model based on stator current, analyzing the representation of localized faults on sun gears, planet gears, and ring gears in the current signal. Furthermore, Chen et al. [19] established a phenomenological model of motor stator current and introduced the adaptive iterative generalized demodulation method for current fault feature extraction, achieving good results under variable operating conditions. Touti et al. [20] utilized MCSA to extract monitoring signal features for wind turbine systems, showing its effectiveness even with low sampling rates and short signal durations. Zhang et al. [21] proposed a hypergraph convolutional neural network based on current time-shifting addition, which successfully applied to intelligent classification and identification of motor-gear coupled system faults. Following this, Zhang et al. [22] introduced a trustable intelligent fusion framework based on modified graph convolutional networks, which integrates multi-channel current signals for fusion diagnosis of electromechanical coupled systems.

The aforementioned studies on planetary gear system dynamics modeling and motor current characterization problems have been somewhat isolated, without considering their combined analysis. In the context of the rapid advancement of wind power equipment and new energy vehicles, the demands for precision, stability, and vibration response of motor-gear systems under dynamic conditions, including acceleration and impact, have significantly increased.

An isolated analysis of gear dynamics fails to account for the interplay between the motor and its control system, leading to limitations in providing accurate system response predictions and a restricted ability to optimize vibration responses. Therefore, it is imperative to comprehensively address the impact of the motor and its control system and establish a holistic electromechanical coupling model for the motor-gear system [8]. In this area, several pioneers have laid the groundwork with their innovative research. For instance, Liu et al. [23] introduced a herringbone planetary gear set dynamics model suitable for analyzing variable-speed processes by incorporating angular displacement in the gear meshing process. Recognizing that the rotational speed of the planetary gearbox is not very high, Bai et al. [24], building on Liu's work, omitted Coriolis and centripetal accelerations in their modeling to investigate the impact of pulse and stable loads on the electromechanical coupled system. Yi et al. [25] established a translational-torsional dynamics model of a planetary gear transmission system using the centralized parameter method, considering a different coordinate system from Liu's approach. This model is suitable for analyzing the dynamic characteristics of gear electromechanical systems under variable speed and load conditions. Xu et al. [26] developed a coupled dynamics model for multistage gearboxes, designed for the analysis of variable-speed processes while accounting for structural flexibility. They expressed time-varying gear meshing stiffness and meshing errors as angular displacement functions of gears and investigated the dynamics of multistage gearboxes during variable-speed operation. Han et al. [2] introduced a magnetic equivalent circuits model and created a coupled gear-motor dynamics model by integrating the motor model and planetary driveline torsion model. They analyzed the response characteristics of gears in different tooth chipping fault states. Shu et al. [27] established a multi-motor drive EMCS and explored the electromechanical coupling characteristics of the multi-motor system under varying speed and load conditions through simulations and experiments. Bilal et al. [28] utilized the elevated energy method to correct time-varying gear meshing stiffness and developed a fixed-axis gear-motor coupling dynamics model. This model was thoroughly verified in normal as well as fault states. Chen et al. [29] established an electromechanical rigid-flexible coupled dynamics model by considering structural flexibility and magnetic saturation characteristics. They analyzed the dynamic characteristics of the model under varying loads and speeds.

In summary, the research discussed above has made significant contributions to the modeling of motor-gear systems and the study of their dynamic characteristics. However, some of the studies simplified the gear system into a basic torsional model with "three masses and two axes," which limits the in-depth exploration of the dynamic response characteristics of the gear system. Other studies, while performing detailed modeling of the gear system, failed to account for the impact of the inverter power supply in the electrical domain and oversimplified the voltage at the motor's input. Furthermore, the representation of time-varying meshing stiffness under variable speed conditions, often depicted as a rectangular or trapezoidal wave, may not accurately reflect the true time-varying nature of the gearbox's meshing stiffness. Consequently, the resulting dynamic responses may contain inaccuracies. Additionally, the effects of non-ideal working conditions, such as inverter switching tube open circuits and power shortages, on the dynamic characteristics of the gear-motor coupling system have received limited attention in existing research.

To address these issues, this paper proposes a planetary drive system dynamics model, which can be used to analyze variable speed processes by considering the internal and external excitation factors, such as time-varying gear mesh stiffness, bearing support stiffness, mesh error; At the same time, a model for the equivalent circuit of a three-phase induction motor is proposed, and a control algorithm based on spatial voltage vectors and a power model for the inverter are introduced. This is then combined with existing translation-torsion models for gear and the complete drive chain of the electromechanical system. The final model is verified for accuracy by analyzing the current and vibration response of the system under steady-state conditions. The mechanism of vibration-current coupling of the gear-electromechanical system under the non-steady state conditions such as uniform speed, sudden change of the power supply frequency and sudden change of the load is revealed, and the dynamic characteristics of the electromechanical system under the non-ideal conditions such as open circuit of the switching tube of the inverter and lack of phase of the power supply are further investigated. The main

contributions of the proposed model for electromechanically coupled systems are as follows.

(1) A comprehensive electromechanical coupling model for the drive chain was developed by integrating translation-torsion models with the motor equivalent circuit model within the electromechanical system.
(2) The coupling mechanism of current-vibration in the system was revealed and the dynamic characteristics under non-steady and non-ideal scenarios was analyzed.
(3) Several experiments were conducted to investigate the dynamics of the electromechanical coupling system within the planetary driveline under various operating conditions. These experiments aimed to validate the accuracy and rationality of the modeling across the time domain, frequency domain, and time–frequency domain. The relevant research results provide a better theoretical basis for the condition monitoring of planetary drive electromechanical coupling system.

The paper is structured as follows: Sect. 2 calculates internal and external excitations under varying speed conditions, incorporating factors like time-varying gear mesh stiffness, bearing support stiffness, and mesh error. In Sect. 3, a translational-torsional dynamics model for the planetary drive system is developed using the centralized parameter method, suitable for analyzing variable operating conditions. It also establishes a refined coupled dynamics model for the complex gear-electromechanical system, incorporating the equivalent circuit model of the asynchronous motor, an inverter power supply model, and a space-voltage vector control algorithm. Section 4 delves into the vibration-current coupling mechanism of the gear-motor system and validates the model's accuracy through comparisons of simulation and experimental results under steady-state conditions. Section 5 explores the vibration-current coupling mechanism of the electromechanical system under non-steady-state conditions, such as constant speed operation, sudden power supply frequency changes, and unexpected load variations, using simulation and experimental results. In Sect. 6, the dynamic characteristics of the electromechanical system are investigated under non-ideal working conditions, including scenarios such as three-phase inverter power supply switching tube open circuits and power supply phase losses.

2 Time-varying excitation analysis of EMCS under variable operating conditions

2.1 Gear meshing stiffness analysis under variable speed condition

The time-varying mesh stiffness (TVMS) is one of the important internal excitations of a gear train. The TVMS changes periodically due to the alternating changes in the number of gear pairs during the meshing process. In the past decades, scholars have carried out extensive research on the calculation methods of gear meshing stiffness [15, 30], among which, the energy method with simple algorithm and obvious physical significance has become the commonly used meshing stiffness calculation method by most scholars. Further, the improved energy method [12, 31] considers the overcurve equation close to the actual one, avoids the judgment of the number of meshing teeth in the process of stiffness calculation, and can effectively improve the calculation accuracy. Therefore, in this paper, the stiffness excitation of the sun gear-planet gear and planet gear-inner ring gear in the planetary transmission system is calculated by the improved energy method. The structural parameters of the planetary gearbox studied in this paper are shown in Table 1.

When the energy method is used to calculate the TVMS, it is usually assumed that the potential energy of the gear in the meshing process consists of five parts: the Hertzian potential energy U_h, the bending potential energy U_b, the radial compression variable potential energy U_a, and the shear variable potential energy U_s. Further, their corresponding stiffnesses can be calculated separately. Combined with Fig. 1, the corresponding Hertzian contact stiffness k_h, bending stiffness k_b, radial compression stiffness k_a, and shear stiffness k_s can be obtained as Eqs. (1)–(5).

$$k_h = \frac{\pi EL}{4(1-v^2)} \tag{1}$$

$$\frac{1}{k_b} = \int_{-\alpha_1}^{\alpha_2} \frac{3\{1+\cos\alpha_1[(\alpha_2-\alpha_1)\sin\alpha-\cos]\}^2(\alpha_2-a)\cos\alpha}{2EL[\sin\alpha+(\alpha_2-\alpha)\cos\alpha]^3} d\alpha \tag{2}$$

$$\frac{1}{k_s} = \int_{-\alpha_1}^{\alpha_2} \frac{1.2(1+v)(\alpha_2-a)\cos\alpha\cos^2\alpha_1}{EL[\sin\alpha+(\alpha_2-\alpha)\cos\alpha]} d\alpha \tag{3}$$

Table 1 Planetary gearbox structural parameters

Parameters	Sun gear	Planet gear	Ring gear	Carrier
Tooth number	17	34(3)	88	–
Tooth width (mm)	26	30	30	–
Addendums (mm)	2.800	3.234	2.714	–
Dedendums (mm)	1.266	0.832	1.318	–
Base circle radius (mm)	31.950	63.899	165.386	–
Modification coefficient	1.234	1.667	1.182	–
Normal module (mm)	2			–
Pressure angle (°)	20			–
Young modulus (Pa)	2.06×10^{11}			–
Poisson ration	0.30			–
Mass (kg)	0.482	0.414	2.202	6.310
Moment of inertia (kg·m^2)	3.4×10^{-4}	2.05×10^{-4}	1.01×10^{-2}	2.73×10^{-2}

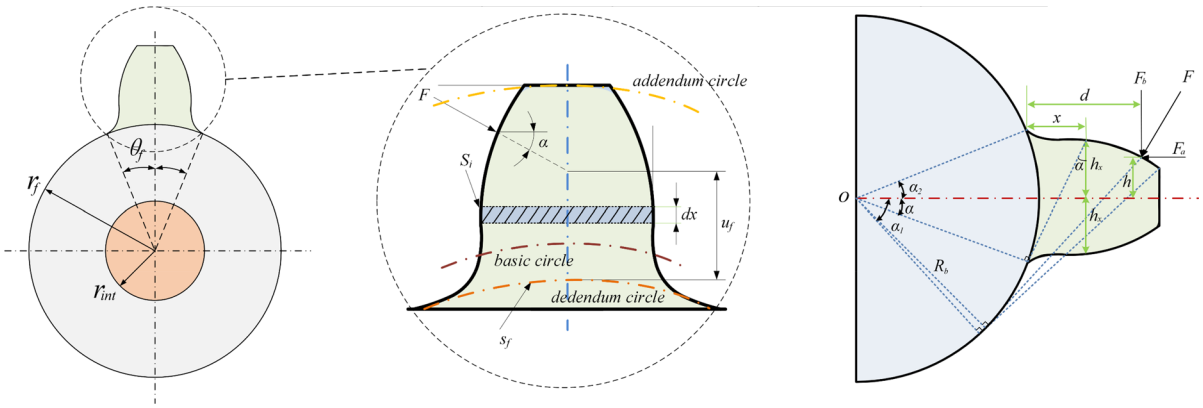

Fig. 1 single tooth force analysis

$$\frac{1}{k_a} = \int_{-\alpha_1}^{\alpha_2} \frac{(\alpha_2 - a)\cos\alpha \sin^2\alpha_1}{2EL[\sin\alpha + (\alpha_2 - \alpha)\cos\alpha]} d\alpha \tag{4}$$

Since external-external gears undergo flexible deformation of their base body during the meshing process [31], it is essential to consider the flexibility deformation stiffness of the gear base body when calculating the overall stiffness, as shown in Eq. (5). The parameters in the equation can be referenced from the literature [31]. It is worth noting that since planet gear-ring gear are external-internal gears, this type of gears is only considered k_h, k_b, k_s, k_a in the process of calculating the total stiffness, and the exact formula can be referred to the literature [15].

$$k_f = \frac{1}{\frac{\cos^2\alpha}{EL}\left\{L' \times \left(\frac{u_f}{s_f}\right)^2 + M' \times \left(\frac{u_f}{s_f}\right) + P' \times (1 + Q' \times \tan^2\alpha)\right\}} \tag{5}$$

The total meshing stiffness when a single pair of gear pair meshes can be obtained by calculating each of the above stiffnesses in series, as shown in Eq. (6).

$$k_{\text{total}} = \frac{1}{\frac{1}{k_h} + \frac{1}{k_{b1}} + \frac{1}{k_{s1}} + \frac{1}{k_{f1}} + \frac{1}{k_{a1}} + \frac{1}{k_{b2}} + \frac{1}{k_{s2}} + \frac{1}{k_{a2}} + \frac{1}{k_{f2}}} \tag{6}$$

When two pairs of gear teeth are involved in meshing at the same time, the meshing stiffness formula is updated to Eq. (7).

$$k_{total} = \sum_{i=1}^{2} \frac{1}{\frac{1}{k_{h,i}} + \frac{1}{k_{b1,i}} + \frac{1}{k_{s1,i}} + \frac{1}{k_{f1,i}} + \frac{1}{k_{a1,i}} + \frac{1}{k_{b2,i}} + \frac{1}{k_{s2,i}} + \frac{1}{k_{a2,i}} + \frac{1}{k_{f2,i}}} \tag{7}$$

where $i = 1$ denotes that the first pair of gear teeth are engaged and $i = 2$ denotes that the second pair of gear teeth are engaged.

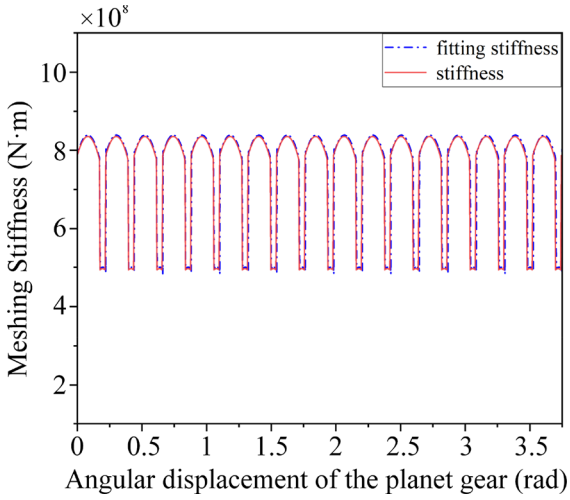

Fig. 2 sun gear-planet gear meshing stiffness

The sun gear-planet gear meshing stiffness is obtained by calculation as shown in Fig. 2. To cater to the diverse requirements of the real operation environment, the working conditions of the transmission system are intricate and changeable. For instance, when the motor undergoes start-stop cycles or operates in a speed-regulation mode, the speed of the transmission system exhibits time-varying characteristics. At this juncture, continuing to employ traditional time-dependent functions to depict the meshing stiffness would undoubtedly introduce challenges when addressing the overall dynamics of EMCS. In the practical operational setting of electromechanical coupling equipment, the motor's angular position is typically known. Employing angle-related functions to represent the meshing stiffness can enhance the applicability of the electromechanical coupling model, especially in non-steady state conditions. Furthermore, to minimize the real-time computational workload associated with meshing stiffness during the simulation process and ensure that the changes in meshing stiffness between components adhere to the prescribed patterns under non-steady state working conditions, we extend the angular domain representation of the calculated meshing stiffness in the form of a Fourier series. The corresponding formula is presented in Eq. (8) [25].

$$\begin{cases} k_{spn}(\theta_{pn}) = a_{spn0} + \sum_{l=1}^{\infty} a_{spnl}\cos\left[l\left(Z_p\theta_{pn} + Z_s\varphi_n + \gamma_n\right)\right] \\ \qquad + \sum_{l=1}^{\infty} b_{spnl}\sin\left[l\left(Z_p\theta_{pn} + Z_s\varphi_n + \gamma_n\right)\right] \\ k_{rpn}(\theta_{pn}) = a_{rpn0} + \sum_{l=1}^{\infty} a_{rpnl}\cos\left[l\left(Z_p\theta_{pn} - Z_r\varphi_n + \gamma_n + \gamma_r\right)\right] \\ \qquad + \sum_{l=1}^{\infty} b_{rpnl}\sin\left[l\left(Z_p\theta_{pn} - Z_r\varphi_n + \gamma_n + \gamma_r\right)\right] \end{cases} \tag{8}$$

where *spn* and *rpn* respectively denote the meshing interaction between the sun gear and the *n*th planet gear, the ring gear and the *n*th planet gear. θ_{pn} represents the rotational angle of the *n*th planet gear; a and b are the coefficients of the Fourier series; l stands for the number of harmonics; Z_p, Z_s and Z_r correspond to the number of teeth on the planet gear, sun gear, and ring gear, respectively.

To accurately represent the actual meshing stiffness, we conducted a 100th order Fourier series fitting to obtain the curve of meshing stiffness as a function of the planet gear angle. The comparison between the sun gear-planet gear stiffness curve derived from the Fourier series fitting and the stiffness curve calculated using the energy method is illustrated in Fig. 2. From the comparison curves, it is evident that the error between the fitted meshing stiffness and the meshing stiffness calculated by the energy method is minimal. To assess this error, the determination coefficient R^2 is employed. The formula for determining the coefficient is provided in Eq. (9). It is worth noting that the determination coefficients for k_{sp} and k_{rp}, calculated through the energy method and through fitting, are 0.971 and 0.964, respectively. This confirms the high accuracy of the fitted stiffness, and its integration into the electromechanical coupled dynamics model is expected to enhance computational precision.

$$R^2 = \frac{\sum_{i=1}^{m}(\hat{y}_i - \overline{y})^2}{\sum_{i=1}^{m}(y_i - \overline{y})^2} = 1 - \frac{\sum_{i=1}^{m}(y_i - \hat{y}_i)^2}{\sum_{i=1}^{m}(y_i - \overline{y})^2} \tag{9}$$

where y_i represents the gear pair mesh stiffness obtained through energy method; $\hat{y}$ is the gear pair mesh stiffness acquired through Fourier series fitting;

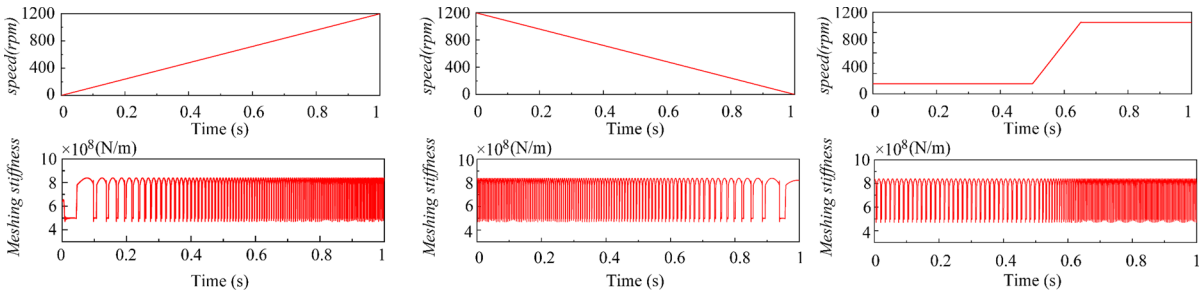

Fig. 3 TVMS of gears under variable speed conditions

$\bar{y}$ denotes the average gear pair mesh stiffness determined through energy method calculation. The coefficient of determination, R^2, measures the goodness of fit, with a higher value indicating a better fitting effect. The optimal value for R^2 is 1, representing a perfect fit.

Under variable speed conditions, the meshing stiffness exhibits the time-varying characteristics. In this context, we consider three operating scenarios: linear speed-up, linear speed-down, and speed regulation. The TVMS under variable speeds is calculated through fitting, as depicted in Fig. 3. The advantage of adopting this fitting method is that it obviates the need for knowledge of the input shaft's speed, and the meshing stiffness adapts itself in accordance with the motor input speed. This aligns with the actual operational process of the motor-gear system. Moreover, unlike much of the existing work that approximates TVMS as a trapezoidal or rectangular wave, our approach bridges the gap between approximation and actual calculation. We utilize the coefficient of determination to evaluate this measure, ensuring a high degree of accuracy in fitting the stiffness. This, in turn, enhances the precision of subsequent dynamic calculations.

2.2 Time-varying bearing stiffness

The traditional approach to analyzing the dynamics of planetary gears has typically treated bearing support stiffness as static support stiffness. However, in the actual operation of planetary gearboxes, different numbers of rollers in the bearings are alternately engaged, leading to time-varying bearing support forces. Among these, the time-varying support stiffness of the sun gear bearing in the planetary gearbox has the most significant impact on the overall system dynamics. Therefore, this study fully incorporates the time-varying support stiffness of the sun gear into the modeling process. Specifically, the time-varying support stiffness of the bearing is modeled using Hertzian contact theory, as illustrated in Fig. 4. The calculation process is based on the following assumptions: (1) no relative sliding occurs between the shaft and the inner ring; (2) there is no relative sliding between the rolling element and the raceway; (3) the outer ring of the bearing is rigidly connected to the gearbox body; and (4) the rolling element undergoes deformation only when subjected to compression.

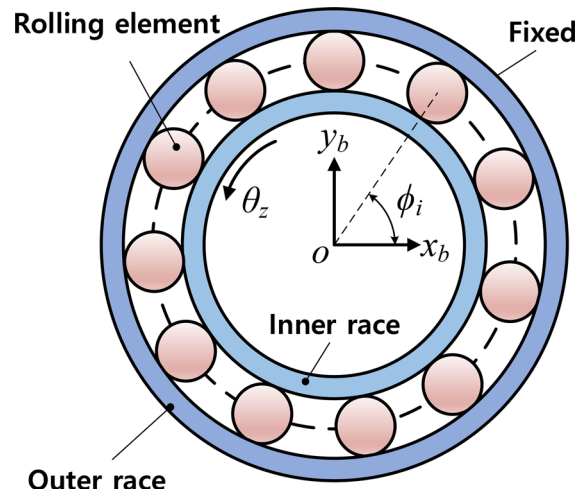

Fig. 4 Bearing analysis model

Taking into account the aforementioned assumptions, the deformation of the bearing primarily results from the contact deformation between the rollers and the inner/outer rings. The contact deformation of the *i*th rolling element can be represented as:

$$\begin{cases} \delta_{bi} = x_b \cos\phi_i + y_b \sin\phi_i \\ \phi_i = \dfrac{2\pi}{N_b}(i-1) + \theta_z, \quad (i = 1, 2, \ldots, N_b) \end{cases} \tag{10}$$

where x_b and y_b represent the displacements of the center of the inner ring of the bearing in the x and y directions, respectively. ϕ_i signifies the angular position of the bearing rollers; N_b denotes the number of rollers in the bearing; θ_z represents the rotation angle of the inner ring of the bearing.

In accordance with Hertz contact theory, the dynamic bearing force resulting from the contact deformation can be expressed as:

$$\begin{cases} F_{bx} = K_c \sum_{i=1}^{N_b} (x_b \cos\phi_i + y_b \sin\phi_i)^{3/2} H(\delta_{bi}) \cos\phi_i \\ F_{by} = K_c \sum_{i=1}^{N_b} (x_b \cos\phi_i + y_b \sin\phi_i)^{3/2} H(\delta_{bi}) \sin\phi_i \end{cases} \tag{11}$$

where Kc represents the Hertzian contact stiffness, which is dependent on the bearing material and contact shape. $H(\delta_{bi})$ is the Heaviside function used to determine whether contact deformation occurs in the ith roller. It equals 1 when the roller deformation δ_{bi} is positive and 0 otherwise.

From Eq. (11), it is evident that calculating the dynamic bearing force requires the outcomes of the gear dynamics model. Conversely, to solve the dynamics model, the dynamic bearing force must be determined, creating a mutual coupling between the two. Directly employing dynamic bearing force calculation would pose greater challenges in modeling the planetary gear system. In this context, dynamic bearing force is utilized to compute the time-varying support stiffness of the bearing. Subsequently, this time-varying support stiffness is incorporated into the dynamics of the planetary gear system to alleviate the modeling complexity. The calculation of bearing time-varying support stiffness can be performed using Eq. (12).

$$[K(t)]_b = \frac{d\mathbf{F}_b}{d\mathbf{x}} = \begin{bmatrix} \dfrac{dF_{bx}}{dx_b} & \dfrac{dF_{bx}}{dy_b} \\ \dfrac{dF_{by}}{dx_b} & \dfrac{dF_{by}}{dy_b} \end{bmatrix} \tag{12}$$

In the support stiffness matrix presented in the above equation, the main diagonal elements are significantly larger than the non-diagonal elements. Consequently, the non-diagonal elements can typically be disregarded. The bearing support stiffness in the x_b and y_b directions can be represented as:

$$\begin{cases} k_{bx} = \dfrac{3}{2} K_c \sum_{i=1}^{N_b} (x_b \cos\phi_i + y_b \sin\phi_i)^{1/2} H(\delta_{bi}) \cos^2\phi_i \\ k_{by} = \dfrac{3}{2} K_c \sum_{i=1}^{N_b} (x_b \cos\phi_i + y_b \sin\phi_i)^{1/2} H(\delta_{bi}) \sin^2\phi_i \end{cases} \tag{13}$$

2.3 Meshing error under variable speed condition

Owing to the presence of different errors in the manufacturing, processing, and assembly processes, the actual meshing tooth profile deviates from the ideal theoretical meshing tooth profile. This discrepancy serves as a primary internal excitation in the gear system. The meshing error considered in this paper is simplified to comprise the cumulative total deviation of tooth pitch and the integrated tangential deviation of a single tooth. It can be viewed as the sum of the rotational frequency error and the meshing frequency error when performing calculations. Its mathematical expression is further formulated using the corner function, as illustrated below [25]:

$$\begin{aligned} e(\theta_{pn}, \theta_i) = {} & E_{ipn} \sin\left(Z_p \theta_{pn} + \mu_i Z_i \varphi_n + \zeta_i + \gamma_n\right) \\ & + E_{pn} \sin\left(\theta_{pn} - \mu_i \alpha + \eta_n\right) \\ & + E_i \sin(\theta_i - \theta_c - \mu_i(\varphi_n - \alpha) + \eta_i) \end{aligned} \tag{14}$$

where γ_n represents the phase difference between internal and external meshing, and its value follows the same pattern as in meshing stiffness. μ denotes the internal and external meshing coefficients, where $\mu = -1$ signifies internal meshing, and $\mu = 1$ denotes external meshing. ξ and η stand for the initial phases of the meshing error; E_{ipn} refers to the synthesized deviation in the tangential direction of one tooth of the gear pair, representing the meshing frequency error. E_{pn} and E_i represent the cumulative total deviation of the pitch of the gears, signifying the rotational frequency error.

3 Electromechanical coupled dynamics model

3.1 Planetary drive system translational torsional dynamics models

This model assumes that the geometric and physical parameters of the three planetary gears within the planetary drive system are identical, while

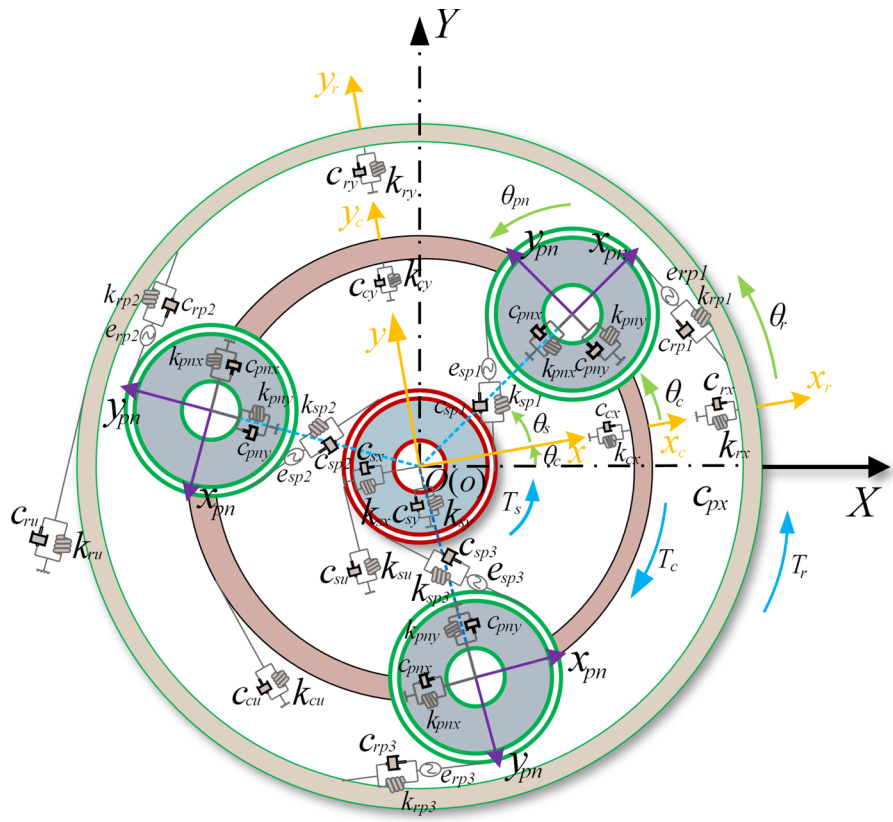

Fig. 5 Planetary gear translational-torsional model

disregarding the influence of the planetary gearbox housings and the flexibility of the planetary carrier. The meshing between gear pairs is simplified as a spring with periodic variations in stiffness corresponding to the angle of rotation. Considering the integrated gear meshing error and the time-varying meshing factor of the gears, the planetary gear translation-torsion dynamics model is established using the lumped parameter method. Each component in the transmission system possesses two translational degrees of freedom and one torsional degree of freedom, the model has a total of 18 degrees of freedom. Multiple coordinate systems are considered in the modeling process: [25] (1) OXY is the fixed coordinate system. (2) The moving coordinate system *oxy* is attached to the planetary carrier. (3) The moving coordinate system $o_{pn}x_{pn}y_{pn}$ fixed on the planet gears.

In actual operation, the rotational speed of the motor is not always predictable, necessitating its consideration when modeling the planetary drive system. The traditional modeling approach often treats each internal and external excitation as a time-dependent function. However, this approach is no longer suitable for the electromechanical coupling model, given that the motor's output is typically represented as rotational angle. The continued use of time to represent corresponding excitation functions would overly complicate the model and increase the complexity of solving dynamics. Moreover, in non-steady-state conditions, the motor's speed may exhibit uniform acceleration, uniform deceleration, sudden changes, and other variations, which impose significant limitations on the traditional planetary translation-torsion model. Hence, it is essential to account for the influence of the motor angle in the modeling process and modify the traditional translational-torsional model. The modified translational-torsional model introduces the angle of each component as a degree of freedom in the torsional direction. Furthermore, all time-related excitation functions are adapted into angle-related excitation functions, resulting in the modified dynamics model illustrated in Fig. 5.

In Fig. 5, θ_s, θ_r, and θ_c represent the angles of rotation for the sun gear, ring gear, and planetary

carrier in the geodetic coordinate system OXY, respectively. Additionally, θ_{pn} is the rotation angle for the planet gear within the dynamic system $o_{pn}x_{pn}y_{pn}$. T_s denotes the input torque applied to the sun gear, while T_c represents the load torque acting on the planetary carrier. This load torque results from the elastic deformation of the motor shaft and the load shaft. φ_n signifies the position angle of the nth planet gear in the OXY coordinate system, calculated as $\varphi_n = 2\pi(n-1)/N$.

Kahraman's research [3] has demonstrated that neglecting the time-varying characteristics of meshing damping does not significantly impact the system's response. Therefore, in this paper, meshing damping is considered to be a constant value, which can be approximated as:

$$c_{mij} = 2\xi_g\sqrt{\frac{\overline{k}_m r_{bi}^2 r_{bj}^2 J_i J_j}{r_i^2 J_i + r_j^2 J_j}} \tag{15}$$

where ξ_g represents the meshing damping ratio, typically within the range of 0.03–0.17. k_m is the average value of meshing stiffness; J_i and J_j are the rotational inertia of the gear; r_i and r_j is the gear pitch circle radius; r_{bi} and r_{bj} are the gear base circle radius.

Considering the geometric relationships outlined in Fig. 5, we can derive the expressions for the meshing deformations (δ_{spn}, δ_{rpn}) between the sun gear and planet gear, as well as between the ring gear and planet gear. Additionally, their corresponding dynamic meshing forces (F_{spn}, F_{rpn}) can be determined in the moving coordinate system oxy as follows:

$$\begin{cases} \delta_{spn} = (x_s - x_{pn})\sin(\varphi_n - \alpha) + (y_s - y_{pn})\cos(\varphi_n - \alpha) \\ \quad + r_s(\theta_s - \theta_c) + r_p\theta_{pn} - e_{spn}(\theta_{pn}, \theta_s) \\ \delta_{rpn} = (x_r - x_{pn})\sin(\varphi_n + \alpha) - (y_{pn} - y_r)\cos(\varphi_n + \alpha) \\ \quad + r_r(\theta_r - \theta_c) - r_p\theta_{pn} - e_{rpn}(\theta_{pn}, \theta_r) \\ F_{spn} = k_{spn}(\theta_{pn})\delta_{spn} + c_{spn}\dot{\delta}_{spn} \\ F_{rpn} = k_{rpn}(\theta_{pn})\delta_{rpn} + c_{rpn}\dot{\delta}_{rpn} \end{cases} \tag{16}$$

Furthermore, considering the influences of tangential acceleration and Koch acceleration, Newton's laws for non-inertial systems are utilized to formulate the equations of translational-torsional dynamics model. The differential equations for the sun gear, ring gear, the nth planet gear (n = 1,2,3), and planetary carrier are sequentially presented in Eqs. (17)–(20):

$$\begin{cases} m_s\left(\ddot{x}_s - 2\dot{y}_s\dot{\theta}_c - x_s\left(\dot{\theta}_c\right)^2 - y_s\ddot{\theta}_c\right) - \sum_{n=1}^{N} F_{spn}\sin(\varphi_n - \alpha) \\ \quad + k_{sx}x_s + c_{sx}\dot{x}_s = 0 \\ m_s\left(\ddot{y}_s + 2\dot{x}_s\dot{\theta}_c - y_s\left(\dot{\theta}_c\right)^2 + x_s\ddot{\theta}_c\right) + \sum_{n=1}^{N} F_{spn}\cos(\varphi_n - \alpha) \\ \quad + k_{sy}y_s + c_{sy}\dot{y}_s = 0 \\ J_s\ddot{\theta}_s + \sum_{n=1}^{3} F_{spn}r_s = T_s \end{cases} \tag{17}$$

$$\begin{cases} m_r\left(\ddot{x}_r - 2\dot{y}_r\dot{\theta}_c - x_r\left(\dot{\theta}_c\right)^2 - y_r\ddot{\theta}_c\right) - \sum_{n=1}^{N} F_{rpn}\sin(\varphi_n + \alpha) \\ \quad + k_{rx}x_r + c_{rx}\dot{x}_r = 0 \\ m_r\left(\ddot{y}_r + 2\dot{x}_r\dot{\theta}_c - y_r\left(\dot{\theta}_c\right)^2 + x_r\ddot{\theta}_c\right) + \sum_{n=1}^{N} F_{rpn}\cos(\varphi_n + \alpha) \\ \quad + k_{ry}y_r + c_{ry}\dot{y}_r = 0 \\ J_r\ddot{\theta}_r - \sum_{n=1}^{3} F_{rpn}r_r + k_{rt}(\theta_r + \theta_c) + c_{rt}\left(\dot{\theta}_r + \dot{\theta}_c\right) = 0 \end{cases} \tag{18}$$

$$\begin{cases} m_{pn}\left(\ddot{x}_n - 2\dot{y}_n\dot{\theta}_c - x_n\left(\dot{\theta}_c\right)^2 - y_n\ddot{\theta}_c\right) - F_{spn}\sin(\varphi_n - \alpha) \\ \quad + F_{rpn}\sin(\varphi_n + \alpha) + k_{pnx}\delta_{pncx} + c_{pnx}\dot{\delta}_{pncx} = 0 \\ m_{pn}\left(\ddot{y}_n + 2\dot{x}_n\dot{\theta}_c - y_n\left(\dot{\theta}_c\right)^2 + x_n\ddot{\theta}_c\right) - F_{spn}\cos(\varphi_n - \alpha) \\ \quad - F_{rpn}\cos(\varphi_n + \alpha) + k_{pny}\delta_{pncy} + c_{pny}\dot{\delta}_{pncy} = 0 \\ J_{pn}\ddot{\theta}_{pn} - F_{spn}r_{pn} + F_{rpn}r_{pn} = 0 \end{cases} \tag{19}$$

$$\begin{cases} m_c\left(\ddot{x}_c - 2\dot{y}_c\dot{\theta}_c - x_c\left(\dot{\theta}_c\right)^2 - y_c\ddot{\theta}_c\right) + \sum_{n=1}^{N} k_{pnx}\delta_{pncx} \\ \quad + \sum_{n=1}^{N} c_{pnx}\dot{\delta}_{pncx} + k_{cx}x_c + c_{cx}\dot{x}_c = 0 \\ m_c\left(\ddot{y}_c + 2\dot{x}_c\dot{\theta}_c - y_c\left(\dot{\theta}_c\right)^2 + x_c\ddot{\theta}_c\right) + \sum_{n=1}^{N} k_{pny}\delta_{pncy} \\ \quad + \sum_{n=1}^{N} c_{pny}\dot{\delta}_{pncy} + k_{cy}y_c + c_{cy}\dot{y}_c = 0 \\ \left(J_c + Nm_p(r_c)^2\right)\ddot{\theta}_c + \sum_{n=1}^{N} k_{pnt}\delta_{pnct}r_c + \sum_{n=1}^{N} c_{pnt}\dot{\delta}_{pnct}r_c = -T_c \end{cases} \tag{20}$$

where δ_{pnx}, δ_{pny}, and δ_{pnt} represent the relative displacements of the planetary gear and the planetary

Table 2 Main parameters of three-phase asynchronous motor

Rated power (kW)	1.5	
Rated voltage (V)	380	
Magnetic pole pair Number (Np)	2	
	Stator	Rotor
Resistance (Ω)	0.42	0.84
d-q axis inductance (mH)	2	2
Moment of inertia (kg·m^2)	–	0.21
Mutual inductance (mH)	68	

carrier in the x, y, and tangential directions, respectively. These displacements can be determined using the positional transformation relationship between the coordinate system oxy and the coordinate system $o_{pn}x_{pn}y_{pn}$:

$$\begin{cases} \delta_{pnx} = x_c - x_{pn} \\ \delta_{pny} = y_c - y_{pn} \\ \delta_{pnt} = (x_{pn} - x_c)\sin\varphi_n - (y_{pn} - y_c)\cos\varphi_n \end{cases} \tag{21}$$

3.2 Three-phase asynchronous motor equivalent model

A three-phase asynchronous motor primarily consists of the stator, rotor, stator winding, and rotor winding. When symmetrical three-phase current is applied to the stator winding, it generates a rotating magnetic field. As a result, the rotor conductor experiences induced electromotive force by cutting through this magnetic field, leading to induced current. The interaction between the rotating magnetic field and the current in the rotor conductor follows Faraday's law, resulting in electromagnetic torque that drives the rotor's rotation. Modeling the motor directly in the three-phase stationary coordinate system introduces numerous coupling parameters and makes it challenging to control motor parameters. Therefore, the *d-q* axis equivalent circuit offers a more effective solution, enabling the skilled decoupling of motor parameters and reducing the complexity of motor modeling. The parameters of the three-phase asynchronous motor are presented in Table 2.

The *d-q* transformation, as illustrated in Fig. 6, essentially involves mapping variables from the three-phase stationary coordinate system *ABC* to the *d-q* rotating coordinate system. This transformation includes both the Clarke transformation and the Park transformation. The Clarke transformation projects variables from the three-phase stationary coordinate system *ABC* into a new coordinate system called the $\alpha\beta$ coordinate system. In the $\alpha\beta$ coordinate system, α and β axes are orthogonal, but i_α and i_β are still sinusoidal. While this transformation simplifies the representation of the variables, it can still be challenging to use PID control. To overcome this challenge, the next step is to transform them into linear quantities, which is the task of the Park transformation. Through the Park transformation, the two-phase stationary coordinates $\alpha\beta$ are converted into the rotating *d-q* coordinates. These coordinates rotate at a speed of ω_s. This transformation simplifies the mathematical model of a three-phase AC motor and makes the control loop more intuitive. In summary, the *d-q* transformation is a fundamental tool in motor control, allowing for a more straightforward representation of motor behavior and improved control system design.

Based on the transformation process described above, the Clarke-Park transformation formulas can be written as:

$$\begin{bmatrix} U_d \\ U_q \end{bmatrix} = \frac{2}{3}\begin{bmatrix} \cos\omega_s t & \cos\left(\omega_s t - \frac{2\pi}{3}\right) & \cos\left(\omega_s t + \frac{2\pi}{3}\right) \\ -\sin\omega_s t & -\sin\left(\omega_s t - \frac{2\pi}{3}\right) & -\sin\left(\omega_s t + \frac{2\pi}{3}\right) \end{bmatrix}\begin{bmatrix} U_A \\ U_B \\ U_C \end{bmatrix} \tag{22}$$

In the d-q-axis coordinate system, the d-q-axis equivalent circuit model can be constructed using the principles of circuit magnetic circuits and the coordinate transformation relationship, as shown in Fig. 7. In the figure, U, I, R, L, and Ψ are vector variables representing voltage, current, resistance, inductance, and magnetic flux, respectively. The subscripts s and r of the vector variables correspond to the variables associated with the stator and rotor of the motor, while the subscripts d and q represent the components projected in the d-q coordinates. L_{ls} and L_{lr} are the equivalent inductances of the stator and rotor in the *d-q* coordinate system's equivalent circuit, respectively. L_m represents the stator-rotor mutual inductance, and ω_r is the motor rotor's angular velocity. The magnetic chain equation, voltage equation, and electromagnetic moment equation, derived from the d-q equivalent circuit diagram, are shown in Eqs. (23)–(25):

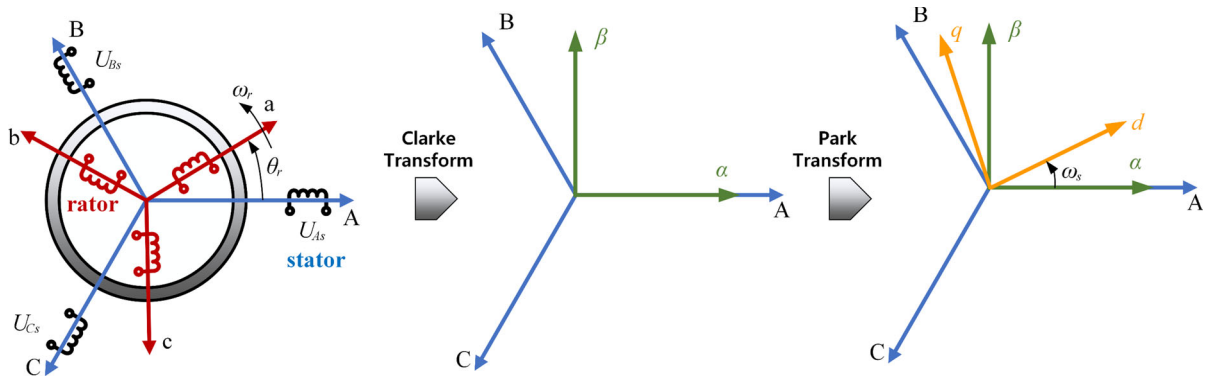

Fig. 6 the schematic diagram of the *d-q* coordinate transformation

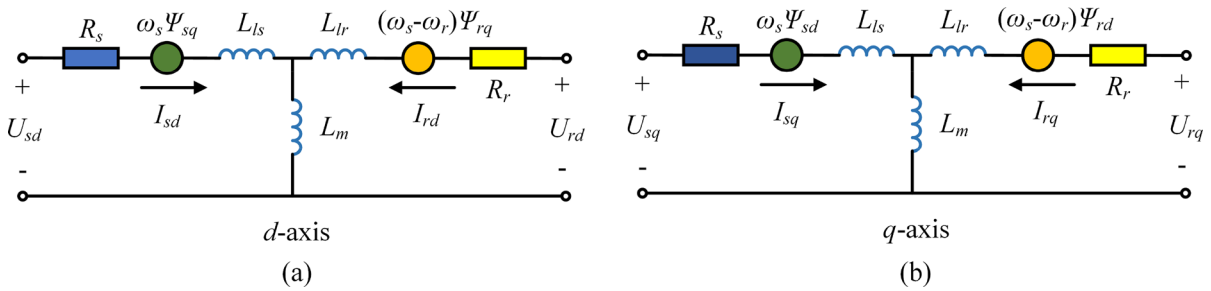

Fig. 7 Schematic diagram of equivalent circuit in d-q coordinate system

$$\begin{cases} \Psi_{sd} = (L_s + L_m)I_{sd} + L_m I_{rd} \\ \Psi_{rd} = (L_r + L_m)I_{rd} + L_m I_{sd} \\ \Psi_{sq} = (L_s + L_m)I_{sq} + L_m I_{rq} \\ \Psi_{rq} = (L_r + L_m)I_{rq} + L_m I_{sq} \end{cases} \tag{23}$$

$$\begin{cases} U_{sd} = R_s I_{sd} + \dfrac{d}{dt}\Psi_{sd} - \omega_s \Psi_{sq} \\ U_{rd} = R_r I_{rd} + \dfrac{d}{dt}\Psi_{rd} - (\omega_s - N_p\omega_r)\Psi_{rq} \\ U_{sq} = R_s I_{sq} + \dfrac{d}{dt}\Psi_{sq} + \omega_s \Psi_{sq} \\ U_{rq} = R_r I_{rq} + \dfrac{d}{dt}\Psi_{rq} + (\omega_s - N_p\omega_r)\Psi_{rd} \end{cases} \tag{24}$$

$$T_e = 1.5N_p(\Psi_{sd}I_{sq} - \Psi_{sq}I_{sq}) \tag{25}$$

3.3 Motor control models

Since the three-phase asynchronous motor model involves more variables and has complex parameter couplings, controlling the motor directly can be challenging. Decoupling the motor system parameters can alleviate this challenge, and vector control of asynchronous motors offers a promising solution. In this paper, rotor magnetic flux directional control mode is employed. In this control mode, the $d-q$ axis rotation frequency is equal to the current frequency, and the magnetic flux Ψ_{rq} on the rotor q-axis remains constant at 0. Under these conditions, the rotor magnetic flux and electromagnetic torque can be simplified as shown in Eq. (26):

$$\omega_s = \omega_r + R_r \frac{L_m}{L_r}\frac{i_{sq}}{\psi_{rd}} \tag{26}$$

$$\psi_r = \psi_{rd} = L_m i_{sd} + \frac{L_m L_r}{R_r}\frac{di_{sd}}{dt} \tag{27}$$

$$T_e = N_p \frac{L_m}{L_r}\psi_{rd} i_{sq} \tag{28}$$

Equation (27) reveals that when the rotor magnetic flux and the direction of the rotor q-axis are always in agreement, the magnetic flux Ψrq on the rotor q-axis remains constant at 0. Under this condition, the rotor magnetic flux on the d-axis is essentially the rotor magnetic flux. It can be observed from the simplified Eq. (28) that at this time, the rotor magnetic flux Ψ_r is only related to the stator current component i_{sd} on the

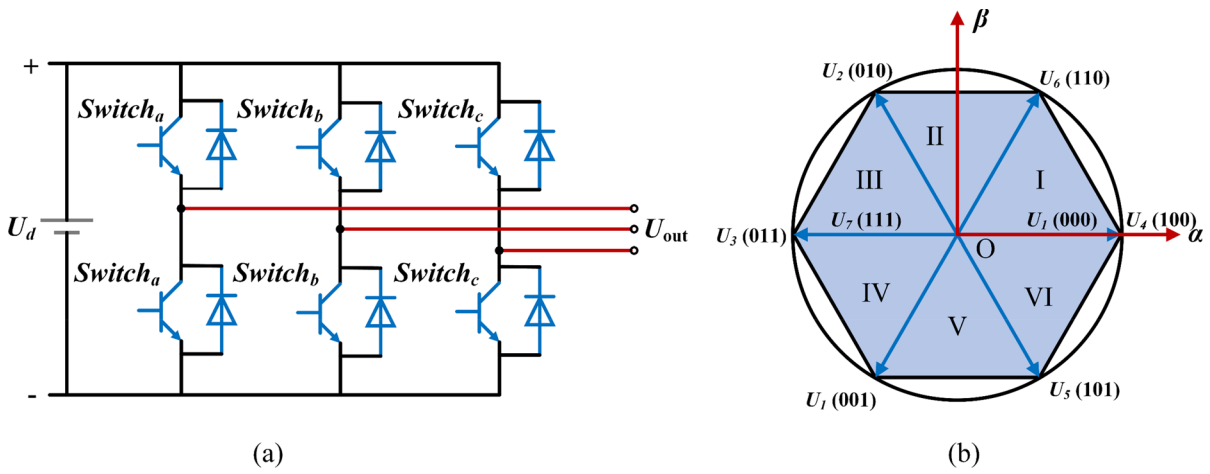

Fig. 8 Schematic diagram of three-phase inverter power supply

d-axis. Furthermore, when using rotor magnetic flux orientation, the electromagnetic torque T_e can be simplified as shown in Eq. (28). From this equation, it's evident that the electromagnetic torque is solely associated with the stator current component i_{sq} on the *q*-axis. Therefore, employing rotor magnetic flux orientation control for asynchronous motors can reduce parameter coupling in the motor system. This method allows separate adjustment of i_{sd} and i_{sq} to control the rotor magnetic flux and electromagnetic torque, thereby enhancing asynchronous motor performance.

The motor's vector control model is depicted in Fig. 8. To ensure the actual current values swiftly converge to the desired reference values, current loop control is commonly employed. The current regulator (ACR) typically incorporates a PI controller. Two PI controllers are used to regulate the *d*-axis and the *q*-axis, respectively. This approach aligns with the projection of the three-phase stationary *ABC* coordinate system into the rotating *d*-*q* coordinate system during the modeling process. Similarly, to rapidly bring the actual rotational speed closer to the reference speed, rotational speed control is also implemented through PI closed-loop control. The rotational speed regulator (ASR) likewise employs a PI controller. The desired speed and target magnetic flux are input and compared with the actual values by the PI controller to generate control currents. These control currents are then fed into the motor controller to execute motor control and drive.

It is worth noting that we incorporate the inverter power supply and the Space Vector Pulse Width Modulation (SVPWM) algorithm into the control method. SVPWM is a recent advancement in Pulse Width Modulation (PWM) techniques and is widely used in motor control systems. It primarily consists of the inverter DC power supply and six power switching elements, as depicted in Fig. 8a. The inverter is equipped with six switches, and the states of the upper and lower bridge switches are always maintained in opposition. These switches are divided into three groups (Sa, Sb, Sc). By arranging and combining the on/off states of these three switch groups, eight different combinations can be obtained, comprising six non-zero vectors (001, 010, 011, 100, 101, 110) and two zero vectors (000, 111). The voltage space vector division is illustrated in Fig. 8b.

The rotor flux orientation control algorithm illustrated in the Fig. 9 operates as follows: Firstly, the three-phase stator current is decomposed into *d*-axis and *q*-axis components using the Park-Clarke transformation. Simultaneously, the actual motor speed is compared with the target motor speed. The obtained signal is sent to the speed control loop for PI control. The resulting signal serves as the reference value for the stator current *q*-axis component (i_{sqe}). A comparison with i_{sqe} yields an output signal sent to the torque current control loop for PI control. The output *q*-axis voltage component (u_{sqref}) is further sent to the SVPWM controller. Similarly, the reference value for the rotor flux is compared with the actual rotor flux

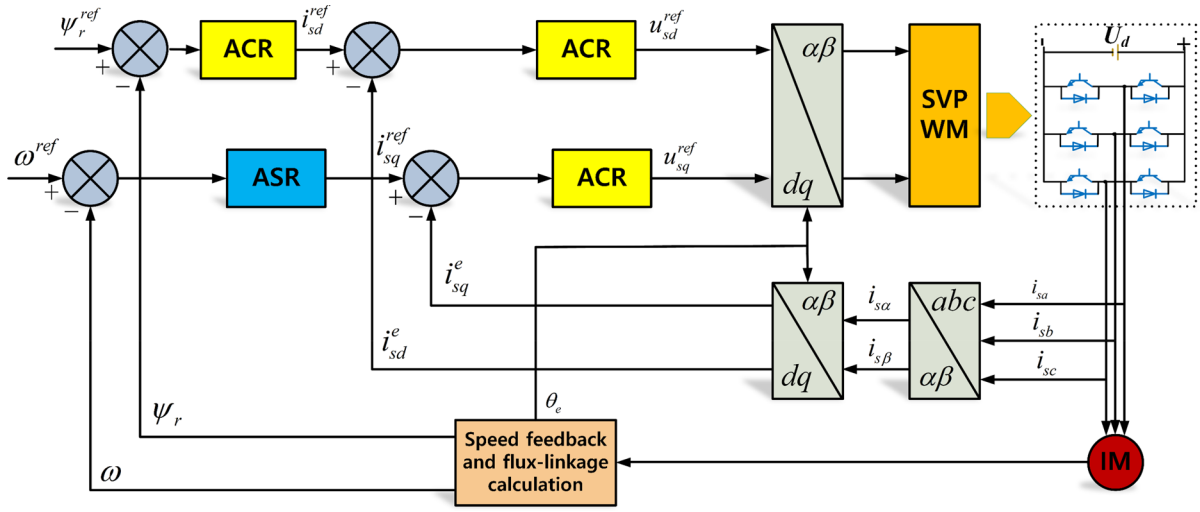

Fig. 9 Schematic diagram of rotor magnetic chain orientation control algorithm

value. The signal is processed by the PI controller to produce i_{sdref}. The signal obtained by comparing i_{sdref} with the actual i_{sde} serves as the input to the current control loop. The d-axis voltage component (u_{sdref}) is generated through PI control and serves as the other input to the SVPWM. At this point, the dq-axis voltage component signals are directed to the SVPWM controller. It generates the pulse waveforms required by the three-phase inverter switching devices using space vector transformation, based on the obtained voltage signals. This process controls the rotational speed of the asynchronous motor to maintain it at the desired reference value, thus completing the rotor flux directional vector control of the asynchronous motor.

The SVPWM output provides a pulse-width-modulated waveform that closely resembles an ideal sinusoidal waveform. This feature allows the rotor magnetic chain vector of the asynchronous motor to trace a trajectory that approximates a circle more closely, resulting in a significant reduction in motor torque pulsation. Furthermore, the SVPWM control algorithm exhibits a higher utilization rate of the DC bus voltage, effectively enhancing the dynamic performance of the motor. In the vector-oriented control system, u_{sdref} and u_{sqref} serve as inputs to the SVPWM controller. The SVPWM controller generates the pulse waveforms required for the inverter switching devices through space vector transformation. This control method maintains the motor speed at the reference value, thereby enabling complete control of the three-phase asynchronous motor.

3.4 Electromechanical coupled dynamics model

In the previous sections, we established the models for the planetary gear translation-torsion system, the three-phase asynchronous motor equivalent circuit, and the motor control system. These components were integrated by implementing rotor magnetic chain-oriented vector control for the asynchronous motor. The asynchronous motor is mechanically linked to the planetary drive system, with the motor rotor connected to the sun gear of the planetary drive system through the motor's output shaft. The output shaft of the planetary drive system is linked to the load side. The electrical system is directly governed by control algorithms for managing the motor's electromagnetic torque, rotor speed, and other parameters. This integration allows for highly efficient and precise control of the gear-motor system. The coupled dynamics model for the planetary gear-motor system is depicted in Fig. 10.

Simplifying the connections between the motor shaft, the planet gear input shaft, the planet gear output shaft, and the load shaft in terms of torsional stiffness and damping, we can express the dynamic equations for both the motor output shaft end and the load end as shown in Eq. (29).

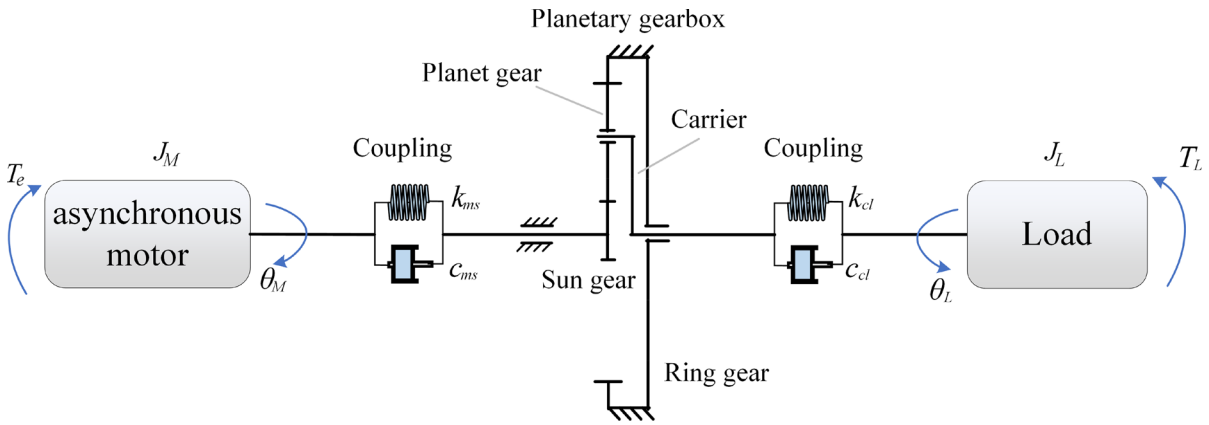

Fig. 10 Motor-gear system dynamics model

$$\begin{cases} J_M\ddot{\theta}_M + c_{ms}(\dot{\theta}_M - \dot{\theta}_s) + k_{ms}(\theta_M - \theta_s) = T_e \\ J_L\ddot{\theta}_L + c_{cl}(\dot{\theta}_L - \dot{\theta}_c) + k_{cl}(\theta_L - \theta_c) = -T_L \end{cases} \tag{29}$$

Taking into account the interconnections between the electrical system and the mechanical components of the motor, as well as the mechanical relationships between the motor shaft and the planetary gearbox, and integrating the dynamics equations of the planetary drive system, the motor magnetic chain equations, the motor voltage equations, and the electromagnetic torque equations, the electromechanical coupling dynamics equations for the planetary drive system are formulated, as demonstrated in Eq. (30).

$$\begin{cases} M\ddot{X} + (C + \dot{\theta}_c G)\dot{X} + (K + \dot{\theta}_c^2 K_t + \ddot{\theta}_c K_a)X = T + E \\ U = RI + \dfrac{d}{dt}\Psi + \omega\Psi \\ \Psi = LI \\ T_e = 1.5n_e\left(\Psi_{ds}I_{qs} - \Psi_{qs}I_{ds}\right) \end{cases} \tag{30}$$

where X is the generalized degree of freedom of the mechanical system; M, C, G, K, Kt, Ka, T, E are the generalized mass matrix, overall damping matrix, gyroscopic matrix, overall stiffness matrix, centripetal stiffness matrix, tangential stiffness matrix, external excitation moment vector, and excitation vector of the meshing error, respectively; and U, R, I, Ψ, ω, and L are the voltage vector, resistance matrix, current matrix, magnetic flux linkage vector, angular velocity vector, and inductance matrix, respectively.

The dynamic equation is used to create a three-phase asynchronous motor model and a directional vector control model within the Matlab/Simulink environment. Additionally, a planetary drive system model is constructed using S-Function, and it is essential to derive the state space representation from Eq. (30) during this modeling process. The electromagnetic torque computed in Simulink is fed into the S-Function as an input, and the real-time rotational speed calculated by the planetary drive system is conveyed to the Simulink motor system. This results in the establishment of a real-time integrated gear-motor dynamics system. The overall process of modeling and experimentally verifying the electromechanical coupled system is illustrated in Fig. 11.

4 Electromechanical coupling dynamics model validation

4.1 Vibration-current coupling mechanism

In a planetary drive EMCS, the vibration and shock generated during the gear meshing process are transmitted to the motor through the motor shaft, leading to an impact on the motor's internal electrical characteristics. As the stiffness of the gear changes with time during the meshing process, the resulting vibration and shock are also intermittent. This causes fluctuations in the motor's output torque to follow a certain pattern. Understanding the vibration and current coupling mechanism is essential for analyzing the dynamics of an electromechanical coupled system. This section utilizes dynamic equations to elucidate the relationship between fluctuations in mechanical system torque and the stator current frequency. This insight provides

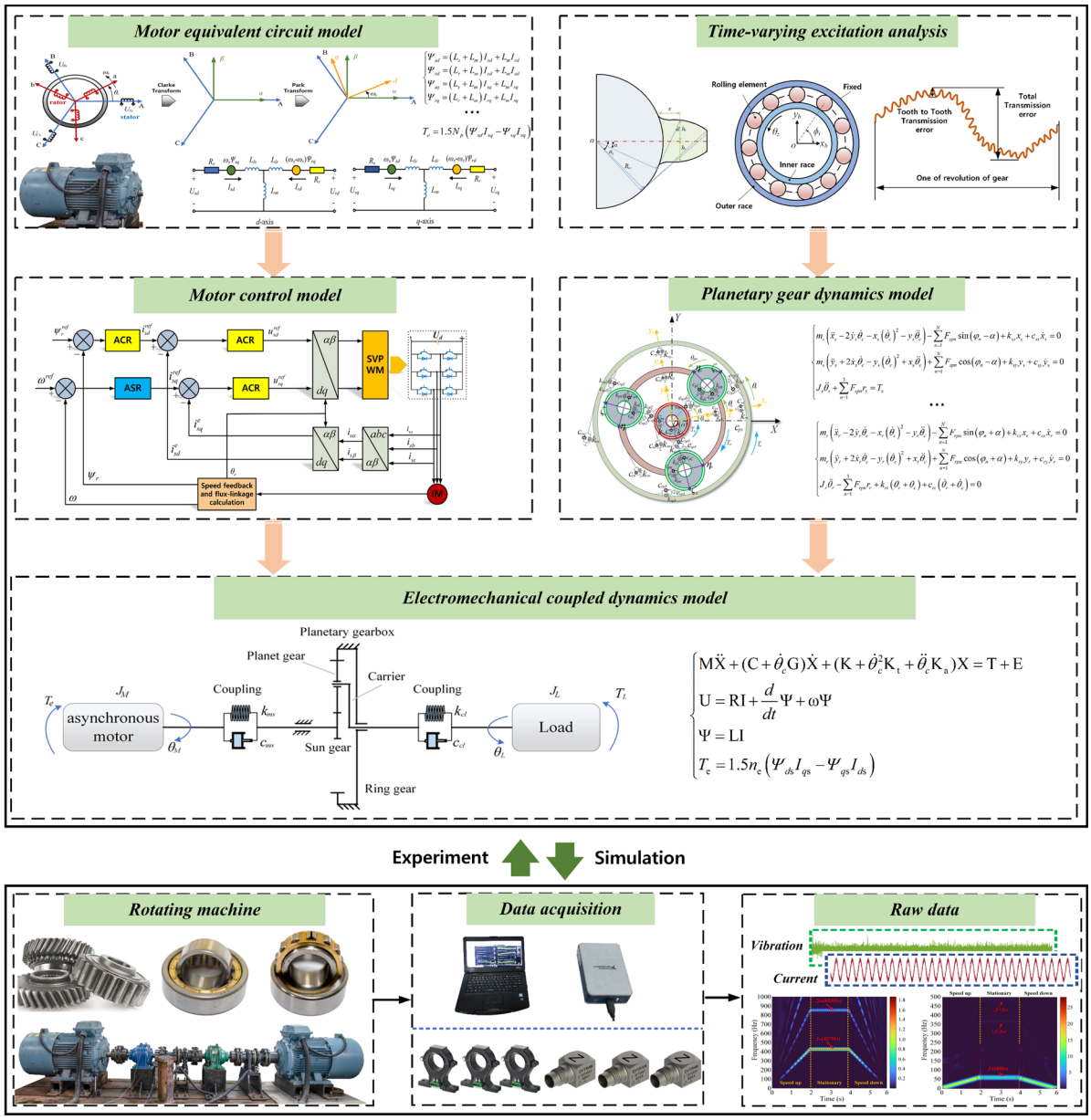

Fig. 11 Overall flow of electromechanical coupled system modeling and experimental verification

a valuable interpretation of the frequency changes observed during simulations and tests.

The load torque T_L at the motor end is assumed to consist primarily of two components: a constant torque and a fluctuating torque. The fluctuating torque is further divided into torque components generated by the rotation of the input shaft T_{input}, the rotation of the output shaft T_{output}, and the meshing of the gears T_m. This relationship is expressed in Eq. (31).

$$\begin{cases} T_{input} = T_{input0}\cos(2\pi f_{input} + \varphi_{input}) \\ T_{output} = T_{output0}\cos(2\pi f_{output} + \varphi_{output}) \\ T_m = T_{m0}\cos(2\pi f_m + \varphi_m) \end{cases} \tag{31}$$

where f_{input}, f_{output}, and f_m are the input shaft rotation frequency, output shaft rotation frequency, and gear mesh frequency, respectively; φ_{input}, φ_{output}, and φ_m are the input shaft phase, output shaft phase, and gear

meshing phase, respectively; T_{input}, T_{output}, and T_m are the peak fluctuating torque generated by the input shaft, output shaft, and gear meshing, respectively.

The torque at the load side of the motor can be determined from the previous equation.

$$\begin{aligned} T_L =& T_0 + T_{input} + T_{output} + T_m \\ =& T_0 + T_{input0}\cos(2\pi f_{input} + \varphi_{input}) \\ &+ T_{output0}\cos(2\pi f_{output} + \varphi_{output}) \\ &+ T_{m0}\cos(2\pi f_m + \varphi_m) \end{aligned} \tag{32}$$

From Eq. (29), it can be observed that when there are fluctuations in the load torque at the motor output shaft end, the motor generates an electromagnetic torque with equal magnitude but opposite phase to maintain the system in equilibrium. The expression for the electromagnetic torque can be represented as:

$$\begin{aligned} T_e =& T_{e0} + T_{ei} + T_{eo} + T_{em} \\ =& T_{e0} + T_{ei0}\cos(2\pi f_{ei} + \varphi_{ei}) + T_{eo0}\cos(2\pi f_{eo} \\ &+ \varphi_{eo}) + T_{em0}\cos(2\pi f_{em} + \varphi_{em}) \end{aligned} \tag{33}$$

where T_{ei}, T_{eo}, T_{em} represent the electromagnetic torque fluctuation components, respectively. T_{ei0}, T_{eo0}, T_{em0} are the amplitudes of each fluctuation component of electromagnetic torque. φ_{ei}, φ_{eo}, φ_{em} are the phases of each fluctuation component of electromagnetic torque.

From Eq. (33), it is evident that the electromagnetic torque contains frequency components that are similar to the mechanical load torque. The electromagnetic torque mainly comprises the input shaft rotational frequency (f_{input}), the output shaft rotational frequency (f_{output}), and the planetary gear meshing frequency (f_m).

Based on the above analysis, it becomes clear that fluctuations in each component of the mechanical torque corresponding to the frequency of each component of the electromagnetic torque result in changes. According to Eq. (25), the fundamental reason for the changes in each component of the electromagnetic torque is due to variations in the magnitude of current or magnetic flux. Similar to the derivation process of electromagnetic torque, by decomposing the current into α and β coordinate systems, each component can be expressed as:

$$\begin{cases} \begin{aligned} i_{s\alpha} =& i_{s\alpha 0} + i_{s\alpha input} + i_{s\alpha output} + i_{s\alpha m} \\ =& A_{s\alpha input}\cos(2\pi f_{input} + \varphi_{s\alpha input}) \\ &+ A_{s\alpha output}\cos(2\pi f_{output} + \varphi_{s\alpha output}) \\ &+ A_{s\alpha m}\cos(2\pi f_m + \varphi_{s\alpha m}) \end{aligned} \\ \begin{aligned} i_{s\beta} =& i_{s\beta 0} + i_{s\beta input} + i_{s\beta output} + i_{s\beta m} \\ =& A_{s\beta input}\cos(2\pi f_{input} + \varphi_{s\beta input}) \\ &+ A_{s\beta output}\cos(2\pi f_{output} + \varphi_{s\beta output}) \\ &+ A_{s\beta m}\cos(2\pi f_m + \varphi_{s\beta m}) \end{aligned} \end{cases}. \tag{34}$$

where $i_{s\alpha 0}$, $i_{s\beta 0}$ denotes the DC component of the α, β axis stator currents; $i_{s\alpha input}$, $i_{s\alpha output}$, $i_{s\alpha m}$ denote the induced currents in the input shaft, output shaft, and gear vibration frequency components, respectively; $\varphi_{s\alpha input}$, $\varphi_{s\alpha output}$, $\varphi_{s\alpha m}$, $\varphi_{s\beta input}$, $\varphi_{s\beta output}$, $\varphi_{s\beta m}$ are the phases of the corresponding induced currents; $A_{s\alpha input}$, $A_{s\alpha output}$, $A_{s\alpha m}$, $A_{s\beta input}$, $A_{s\beta output}$, $A_{s\beta m}$ are the amplitudes of the corresponding induced currents.

The stator phase current i_a can be expressed as:

$$i_a = i_{s\alpha}\cos(2\pi f_e t) + i_{s\beta}\cos(2\pi f_e t) \tag{35}$$

Assuming that $\varphi_{s\alpha} \approx \varphi_{s\beta}$, the above two equations can be simplified as:

$$\begin{aligned} i_a =& i_0\cos(2\pi f_e t - \varphi_0) + \frac{1}{2}(A_{s\alpha input} - A_{s\beta input})\cos(2\pi(f_e + f_{input})t + \varphi_\alpha) \\ &+ \frac{1}{2}(A_{s\alpha input} + A_{s\beta input})\cos(2\pi(f_e - f_{input})t + \varphi_\alpha) + \\ &\frac{1}{2}(A_{s\alpha output} - A_{s\beta output})\cos(2\pi(f_e + f_{output})t + \varphi_\alpha) \\ &+ \frac{1}{2}(A_{s\alpha output} + A_{s\beta output})\cos(2\pi(f_e - f_{output})t + \varphi_\alpha) + \\ &\frac{1}{2}(A_{s\alpha m} - A_{s\beta output})\cos(2\pi(f_e + f_{output})t + \varphi_\alpha) \\ &+ \frac{1}{2}(A_{s\alpha input} + A_{s\beta input})\cos(2\pi(f_e - f_{input})t + \varphi_\alpha) \end{aligned} \tag{36}$$

where $i_0 = \sqrt{i_{s\alpha 0}^2 + i_{s\beta 0}^2}$; $\varphi_0 = \tan^{-1}(i_{s\alpha 0}/i_{s\beta 0})$.

Equation (36) demonstrates that during the operation of the motor-gear system, various frequency components such as $|f_e \pm f_{input}|$, $|f_e \pm f_{output}|$, $|f_e \pm f_m|$ will be present in the stator current spectrum. This analysis helps in understanding and interpreting the simulation and test results more effectively.

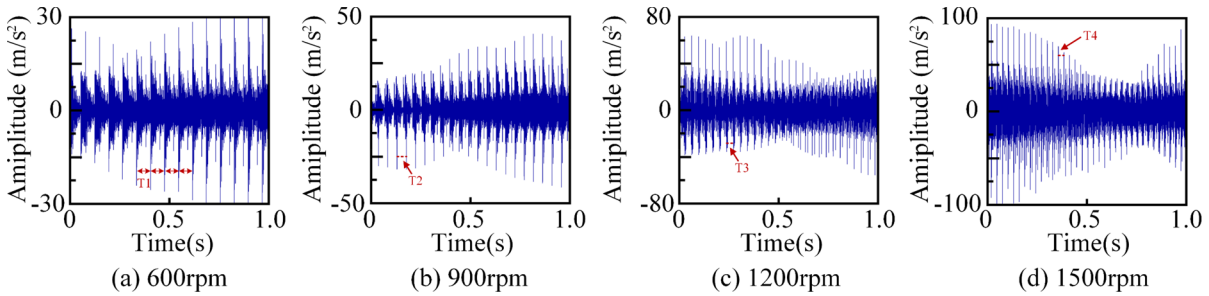

Fig. 12 Time-domain waveforms of ring gear's *Y*-direction vibration acceleration at different steady-state speeds

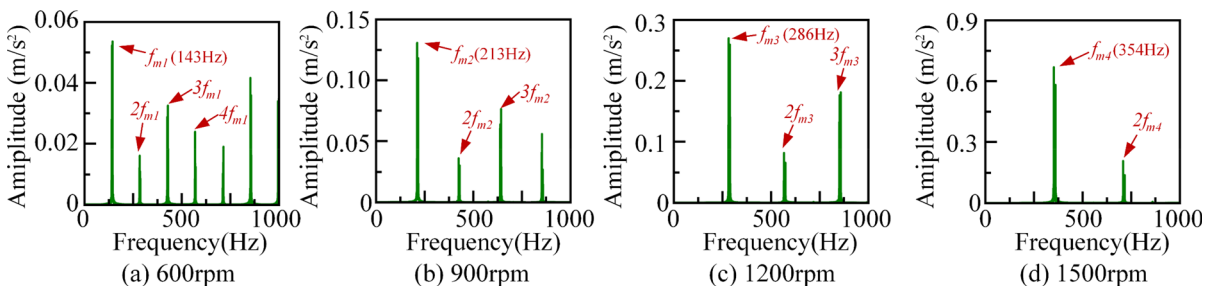

Fig. 13 Spectrum of ring gear's *Y*-direction vibration acceleration at different steady-state speeds

4.2 Dynamic response of motor-gear system under different speed conditions

To validate the accuracy of the established electromechanical coupling model and compare the dynamic characteristics of the electromechanical system under different steady-state working conditions, four sets of steady-state speed conditions were configured at 600, 900, 1200, and 1500 RPM for simulation. The goal was to investigate the mechanical vibration response of the motor-gear system and the variations in the stator current of the motor under these different steady-state speed conditions. All settings for the four working conditions, except for the rotational speed, remained the same. The load applied to the mechanical device (planetary gearbox) was set to 12 N·m, and a simulation step size of 0.00001 s was used with the ode4 Runge–Kutta algorithm for solving. Under these four rotational speed conditions, the vibration accelerations in the x and y directions in the moving coordinate system oxy were simulated and transformed into the geodetic coordinate system OXY in the Y direction. The obtained vibration accelerations in the Y direction of the planetary gearbox at different rotational speeds after transformation are presented in Fig. 12, while the vibration acceleration spectra are shown in Fig. 13.

Analyzing the mechanical system vibration acceleration time-domain waveforms, we observe a clear increase in amplitude as the rotational speed rises. These vibration responses in the time domain consist of two alternating shocks with varying magnitudes. Under the four working conditions, the periods of strong shocks, denoted as T1, T2, T3, and T4, correspond to frequencies of f_{m1} (143 Hz), f_{m2} (213 Hz), f_{m3} (286 Hz), and f_{m4} (354 Hz), respectively. These frequency distributions closely match the theoretical results, validating the accuracy of the mechanical dynamics model. Subsequently, the time-domain waveforms of the motor stator current under the four speed conditions are extracted, as shown in Fig. 14.

The time-domain waveform of the motor stator current remains relatively stable and sinusoidal, with no significant change in amplitude. However, as the rotational speed increases, the power supply frequency gradually becomes higher. As a result, a spectral analysis of the current time-domain signal was conducted to obtain the motor current spectrum, depicted in Fig. 15. For comparison, the theoretically

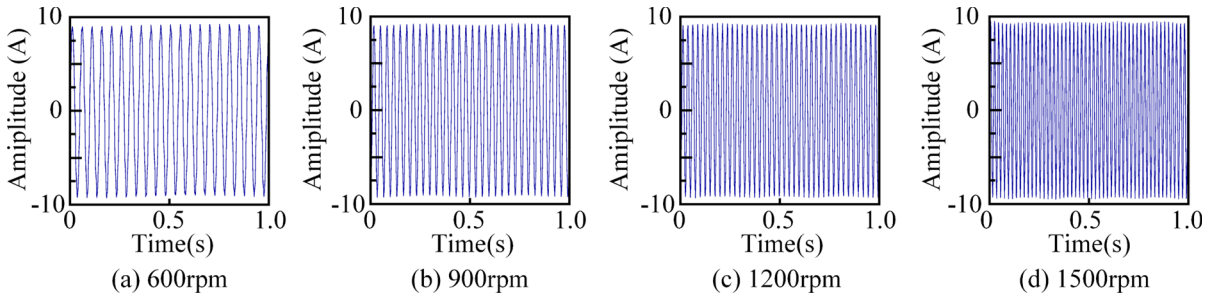

Fig. 14 Time-domain waveforms of motor current at different steady-state speeds

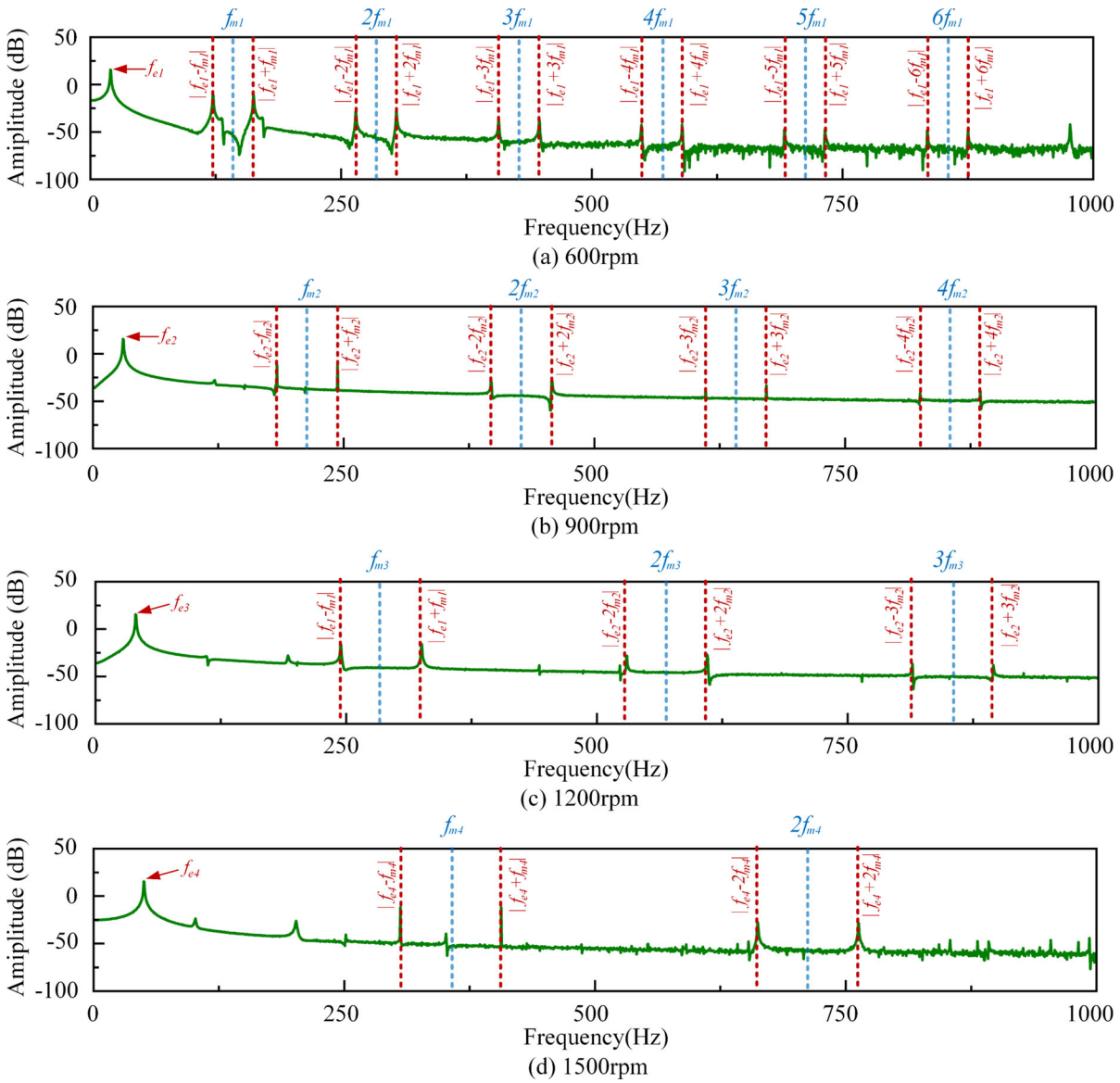

Fig. 15 Motor stator current spectrum at different steady state speeds

Table 3 Main frequencies of vibration and current spectra at different rotational speeds (bold indicates theoretically calculated frequencies)

	f_m (Hz)	f_e (Hz)	$f_e - f_m$ (Hz)	$f_e + f_m$(Hz)	$f_e - 2f_m$ (Hz)	$f_e + 2f_m$ (Hz)
10 Hz	**142.6** (143.1)	**20** (20.2)	**122.6** (122.5)	**162.6** (163.1)	**265.2** (265.6)	**305.2** (305.6)
15 Hz	**213.9** (213.7)	**30** (30.4)	**183.9** (183.7)	**243.9** (244.3)	**397.8** (397.3)	**457.8** (457.6)
20 Hz	**285.3** (285.8)	**40** (40.3)	**245.3** (245.1)	**325.3** (325.2)	**530.6** (530.3)	**610.6** (610.1)
25 Hz	**356.6** (356.3)	**50** (50.1)	**306.6** (306.1)	**406.6** (406.7)	**663.2** (662.6)	**763.2** (762.5)

calculated power supply frequency and the main frequency components are listed in Table 3.

When the electromechanically coupled system operates at a steady rotational speed, its spectral components are mainly composed of the power supply frequency (*fe*) and combinations of the power supply frequency with the meshing frequency, lfe ± nfml. The power supply frequency dominates the spectrum, and the related frequencies in the high-frequency part are less prominent. This is because of the relatively large rotational inertia of the motor rotor and the inductance generated by the motor stator windings, which makes the motor system less sensitive to high-frequency excitations and gives it low-pass filtering characteristics. The calculated theoretical frequencies and the simulation results exhibit good consistency. Under different rotational speed conditions, changes in the power supply frequency and meshing frequency cause shifts in the main frequency of the motor stator current. This feature provides a theoretical basis for state monitoring based on the motor stator current and further validates the accuracy of the established motor-gear system coupled dynamics model.

4.3 Experimental validation

To further validate the accuracy of the established electromechanical coupling dynamics model, we conducted dynamic testing of the electromechanical system under both steady-state and unsteady conditions using the planetary drive electromechanical coupling test rig. The test rig is primarily comprised of a drive system, a transmission system, a loading system, and a signal acquisition system. The drive system consists of a three-phase asynchronous motor and a frequency converter, which allows regulation of the motor speed to achieve various constant speed conditions and sudden changes in power frequency. The transmission system is primarily composed of an NGW planetary gearbox. The loading system includes a magnetic powder brake and a tension controller, with the tension controller adjusting the current to control the load on the planetary gearbox. Sudden changes in load conditions can also be programmed through the tension controller. The signal acquisition system comprises a speed sensor, three vibration acceleration sensors, three Hall current sensors, a data acquisition card, a laptop, and acquisition software. A photoelectric speed sensor is positioned between the drive motor and the gearbox to collect speed pulse signals from the motor's output shaft. The three vibration acceleration sensors are placed at key locations within the planetary gearbox, including the input shaft, the upper end of the bearing, and the upper end of the ring gear. Additionally, three Hall current sensors are positioned at the input shaft of the planetary gearbox, the upper end of the bearing at the output shaft position, and the upper end of the ring gear. At the start of the test, all seven channels simultaneously collect rotational speed pulses, motor current, and gearbox vibration acceleration signals during the operation of the electromechanical system. The sampling rate for all channels is set to 12800 Hz, and the rotational speed and load conditions are determined based on the specific working scenarios. In addition, in order to better control the influence of external noise on the experimental results, we set up the test rig in a semi-anechoic chamber. The schematic diagram of the planetary drive electromechanical coupling test bench is depicted in Fig. 16.

The vibration signals of the gearbox and the motor current signals were collected under four steady-state conditions: 600, 900, 1200, and 1500 rpm. The gearbox load was maintained at 12 N-m for all conditions, and the data collection time was set to 30 s. To emphasize the time-domain information of the

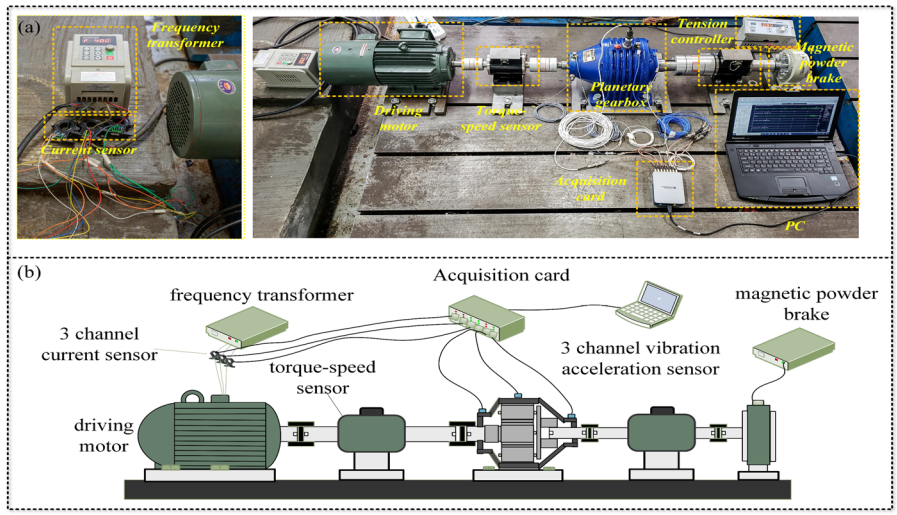

Fig. 16 Dynamics of gear-motor coupled system test rig. **a** Test site diagram; **b** schematic diagram of the test rig

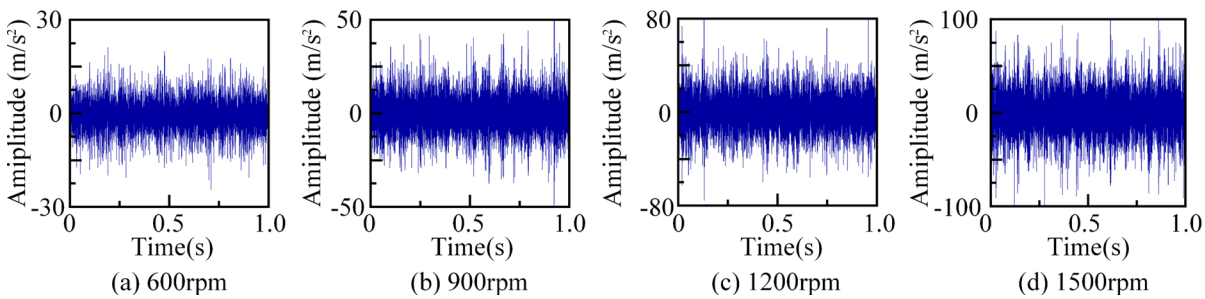

Fig. 17 Time domain waveforms of gearbox vibration acceleration at different steady state speeds (experimental results)

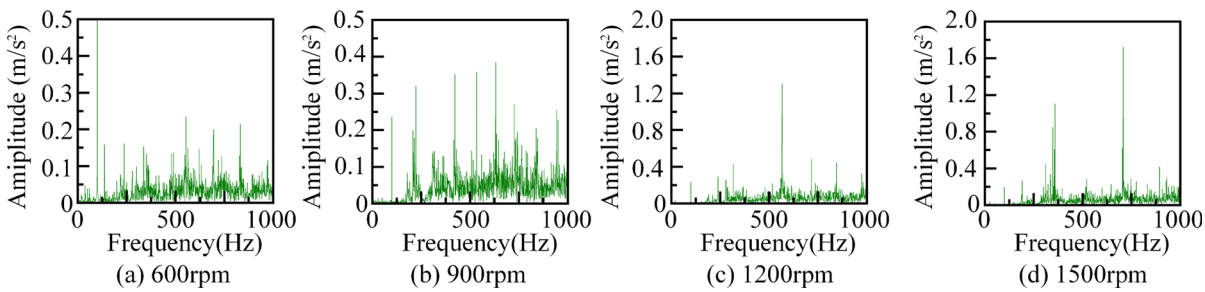

Fig. 18 Gear vibration acceleration spectra at different steady state speeds (experimental results)

vibration and current signals, a portion of the collected signals was selected for analysis. The time-domain waveforms of the gearbox vibration signals under the four steady-state conditions are displayed in Fig. 17.

The time-domain waveforms reveal that as the rotational speed increases, the amplitude of the vibrations also increases. The vibration response in the time-domain waveform consists of two types of alternating shocks with varying intensities. The magnitude of the gear vibration amplitude under the four steady-state working conditions closely matches the simulation results. The frequency spectrum, obtained by Fourier transforming the time-domain signals, is presented in Fig. 18. The spectrum primarily includes the rotational frequency (f_c), gear meshing frequency (f_m), and its harmonics (nf_m), along with their combined components ($nf_m \pm kf_c$). The main frequency distributions in the experimental results

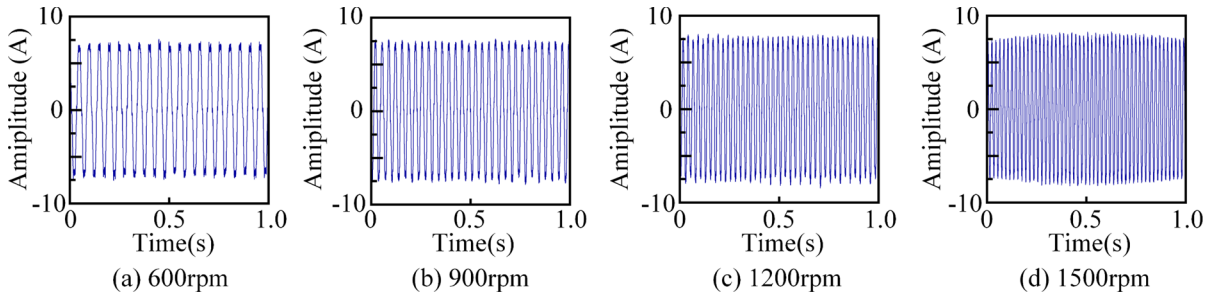

Fig. 19 Time domain waveforms of motor stator current at different steady state speeds (experimental results)

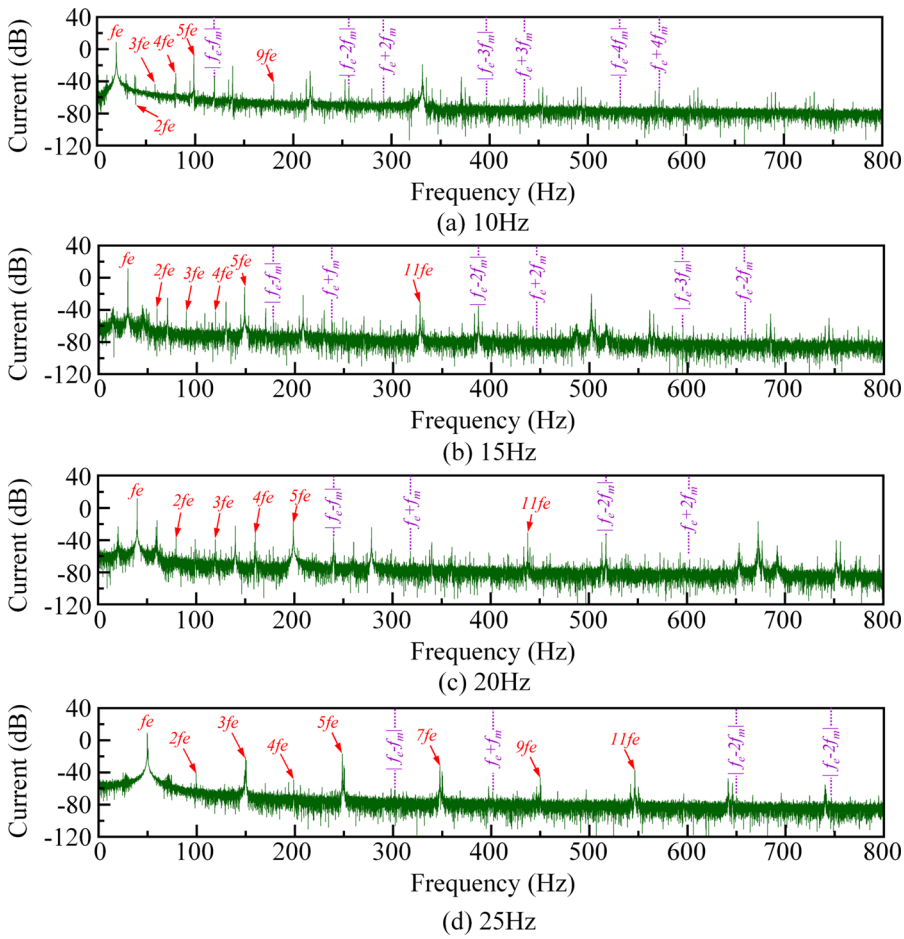

Fig. 20 Spectrogram of motor stator current at different steady state speeds (experimental results)

closely resemble those of the simulation results, confirming the accuracy of the established model.

Subsequently, the time-domain waveforms of the motor stator current under the four different rotational speed conditions are presented in Fig. 19. The motor stator current exhibits relatively stable time-domain waveforms, and the amplitude remains relatively consistent. However, as the rotational speed increases, the power supply frequency gradually becomes larger. This observation aligns with the system simulation results discussed in Sect. 4.2. The Fourier transform of the current signal is displayed in Fig. 20. It is evident from the motor current spectrum that when the electromechanically coupled system operates at a stable rotational speed, the power supply frequency (nf_e) is prominently visible in the stator current

spectrum, with the power supply frequency (f_e) being the dominant component. This presence is attributed to the existence of harmonic interference in the actual power supply. Additionally, the power supply frequency contains components like ($f_e \pm f_m$). This phenomenon arises from the transmission system transmitting the electromagnetic torque through the motor shaft, leading to corresponding frequency modulation in the stator current. The presence of higher-frequency components is not as pronounced, which aligns with the findings of the simulation analysis. The frequency spectrum calculated through experimentation closely matches the simulation spectrum, providing further validation for the accuracy of the established motor-gear system coupled dynamics model. This sets the stage for investigating the dynamic characteristics of the electromechanically coupled system under unsteady conditions.

5 Dynamic characteristics of PMCS under unsteady conditions

Once the dynamics model of the motor-gear coupling system has been established using Simulink, non-stationary working conditions can be configured. These conditions include variations in uniform speed, abrupt changes in power supply frequency, and sudden alterations in the load. This enables the exploration of the relationship between mechanical vibration, motor stator current, and electromagnetic torque under different dynamic working conditions.

5.1 Uniform speed conditions

The operation of a motor-gear system in real-world scenarios typically involves three stages: startup, steady operation, and shutdown. Each of these stages corresponds to specific working conditions. ① Startup stage: this stage typically involves uniform acceleration. The motor's target speed is gradually increased within the motor's response range, allowing the motor to accelerate uniformly from its initial state to the desired speed. ②Stable stage: during this stage, the motor operates at a stable, constant speed, which is the desired working speed. The system may remain in this stage for an extended period, such as during normal operation. ③Shutdown stage: the shutdown stage usually corresponds to uniform deceleration. In this stage, the motor's target speed is gradually reduced to zero, causing the motor to decelerate uniformly before coming to a stop. These stages and working conditions are essential considerations for understanding the behavior of motor-gear systems in practical applications.

5.1.1 Simulation analysis results

To study the start-stop response of the motor-gear system under uniform speed conditions, a simulation scenario was created where the motor's speed rapidly increased from 0 to 1800 rpm within 2 s and then decreased from 1800 rpm to 0 after maintaining a stable speed of 1800 rpm for 2 s. The entire start-stop process had a duration of 6 s, and the mechanical load was set to 12 N·m. At the end of the simulation, the system's electromagnetic torque, vibration response, and stator current response were recorded and visualized in Fig. 21. This simulation provides insights into how the system behaves during rapid changes in motor speed and the associated effects on torque, vibrations, and current.

During the 0–2 s phase, as the motor initiates startup, the set target speed gradually increases, creating a deviation from the actual speed. Consequently, the torque current, denoted as i_{sq}, experiences an impact due to this deviation, leading to a rise in electromagnetic torque T_e. Since the load remains consistently at a fixed value, the total torque generated exceeds the load torque, which sets the motor rotor into a phase of uniform acceleration. Throughout this period of uniform acceleration, the target speed of the motor steadily increases, and the deviation from the actual speed remains constant. This maintains the electromagnetic torque T_e at a relatively stable level, facilitating uniform acceleration of the motor rotor. Between 2 and 4 s, as the system reaches a steady state with a target speed of 1800 rpm, the motor's target speed closely matches the actual speed, resulting in a smaller deviation. Consequently, both the torque current i_{sq} and electromagnetic torque T_e decrease, allowing the motor rotor to maintain a state of uniform rotation. The final phase, occurring between 4 and 6 s, represents the gradual shutdown of the motor. During this deceleration phase, the motor's target speed gradually decreases, introducing a deviation from the actual speed, but in the opposite direction compared to the acceleration phase. This deviation influences the

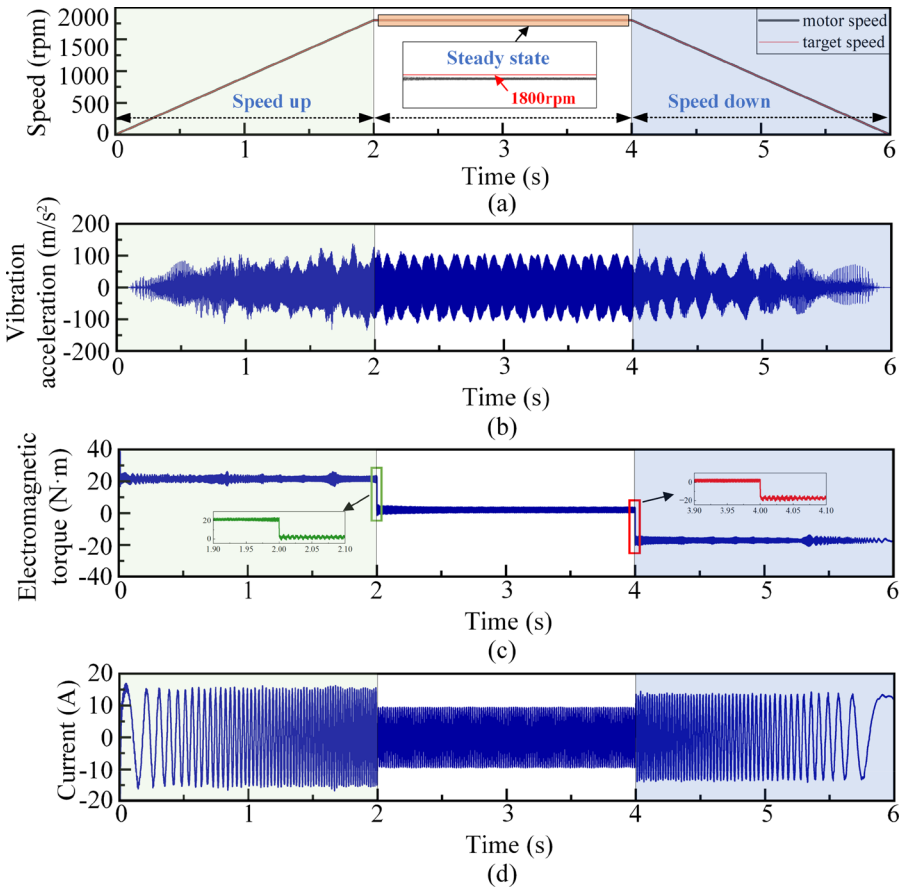

Fig. 21 Dynamic response of electromechanical system under uniform speed condition. **a** Rotation speed. **b** Vibration acceleration. **c** Electromagnetic torque. **d** Current

torque current i_{sq} output by the PI controller in the speed loop, leading to an increase in electromagnetic torque T_e, although in the opposite direction to that observed during uniform acceleration. As the load remains consistently at a fixed value, the combined torque once again exceeds the load torque, initiating uniform deceleration of the motor rotor. In this phase, the motor's target speed uniformly decreases, and the deviation from the actual speed remains constant, maintaining the electromagnetic torque T_e at a relatively stable level to facilitate uniform deceleration of the motor rotor.

To explore the frequency distribution patterns of the dynamic response in the motor-gear system under variable speed conditions while addressing the phenomenon of frequency aliasing resulting from the Fourier transform of vibration and current signals, the short-time Fourier transform (STFT) is employed for both the vibration and current signals. This analysis allows for an investigation of the electromechanical system's response under conditions of uniform acceleration and deceleration in the time–frequency domain. In the STFT spectra represented in Fig. 22a for the vibration signal, the meshing frequency f_m and its octave frequencies, originating from the mechanical drive system, are clearly observable. Furthermore, the meshing frequency follows the rotational speed variations as expected. On the other hand, in Fig. 22b, which presents the STFT for the motor stator current, the power supply frequency f_e is the dominant component. This power supply frequency aligns with the motor's speed variations. Additionally, it's important to note that the power supply frequency f_e can be influenced by the meshing frequency f_m in the mechanical drive system. As a result, two frequency bands, $|f_m \pm f_e|$, are also noticeable in the graph, corroborating the findings presented in Sect. 4.1 and providing further support for the establishment of the mapping relationship between the mechanical drive system and the motor's current. It is also worth

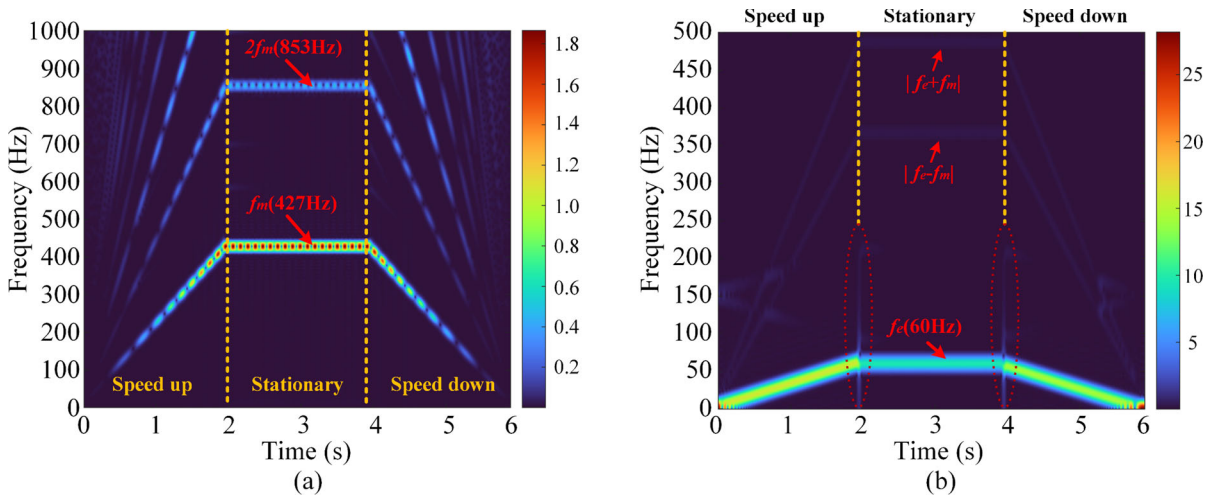

Fig. 22 Time–frequency spectrum of dynamic response of electromechanical system under uniform speed condition. **a** Vibration signal STFT spectrum. **b** Current signal STFT spectrum

mentioning that, in the time–frequency plot of the stator current, notable spikes can be observed at the 2-s and 4-s marks, highlighted by the red circles. These spikes coincide with moments of sudden changes in current amplitude at 2 s and 6 s, corresponding to alterations in rotational speed.

5.1.2 Experimental analysis results

In order to validate the simulation results of the EMCS under uniform speed conditions, experimental tests were conducted on the test bench. It is important to note that, for safety reasons, the motor speed was adjusted to accelerate from 0 to 1800 rpm over 10 s, then decelerate to 0 after maintaining a steady speed at 1800 rpm for 10 s. The entire speed change process had a duration of 30 s. At a sampling rate of 12,800 Hz for all channels, various time-domain signals were obtained. These signals include the rotational speed, gearbox vibration acceleration, and motor stator current during uniform speed variation, as shown in Fig. 23.

In Fig. 23a, the rotational speed pulse signals collected by the photoelectric rotational speed sensor are presented. The corresponding rotational speed curves, marked by the red line in Fig. 23b, align with the experimental setup, confirming the accuracy of the speed changes. Figure 23c displays the time-domain waveform of the gearbox vibration acceleration, where the amplitude of vibration acceleration follows a pattern consistent with the speed changes. During the initial 0–10 s, the vibration amplitude gradually increased, stabilized for the subsequent 10 s, and then gradually decreased. Figure 23d shows the time-domain waveform of the motor stator current, which was acquired through the Hall current sensor. During the first 0–10 s, the current waveform gradually became denser, with an increasing amplitude. This behavior is attributed to the motor's initial start-up, where a significant deviation between the motor's target speed and its actual speed led to increased current output through the control system feedback. Once the motor speed reached a stable value, and the actual speed closely matched the target speed, the current amplitude gradually reduced. During this period, the motor maintained a uniform rotational state. The process of slowing down the motor exhibited a similar pattern, with current amplitudes increasing momentarily at the instant of deceleration and then gradually decreasing. The experimental results of the motor stator current and gearbox vibration acceleration time-domain waveforms during the variable speed process demonstrate a consistent amplitude magnitude and change pattern with the simulation analysis results, thus validating the simulation findings.

The variable speed condition is unique compared to steady-state conditions, and the traditional spectral analysis methods may not be suitable. To address this, similar to the simulation analysis, the short-time

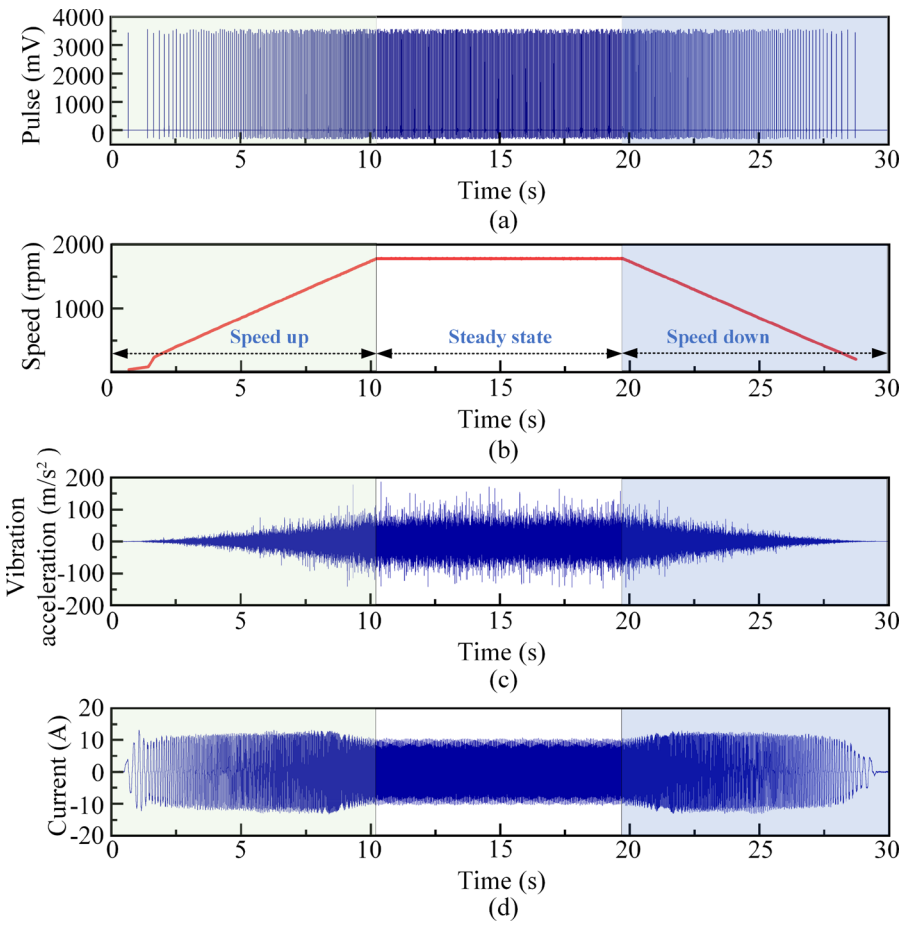

Fig. 23 System response under uniform speed condition (test results). **a** Rotation speed pulse signals. **b** Rotation speed. **c** Vibration acceleration. **d** Current

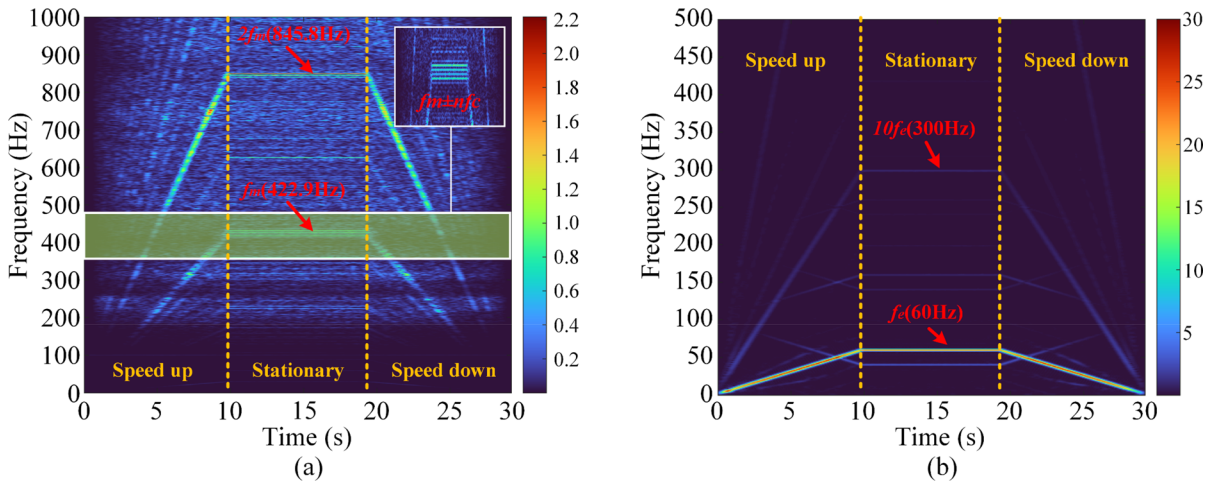

Fig. 24 Time–frequency spectrum of dynamic response of electromechanical system under uniform speed condition. **a** Vibration signal STFT spectrum. **b** Current signal STFT spectrum

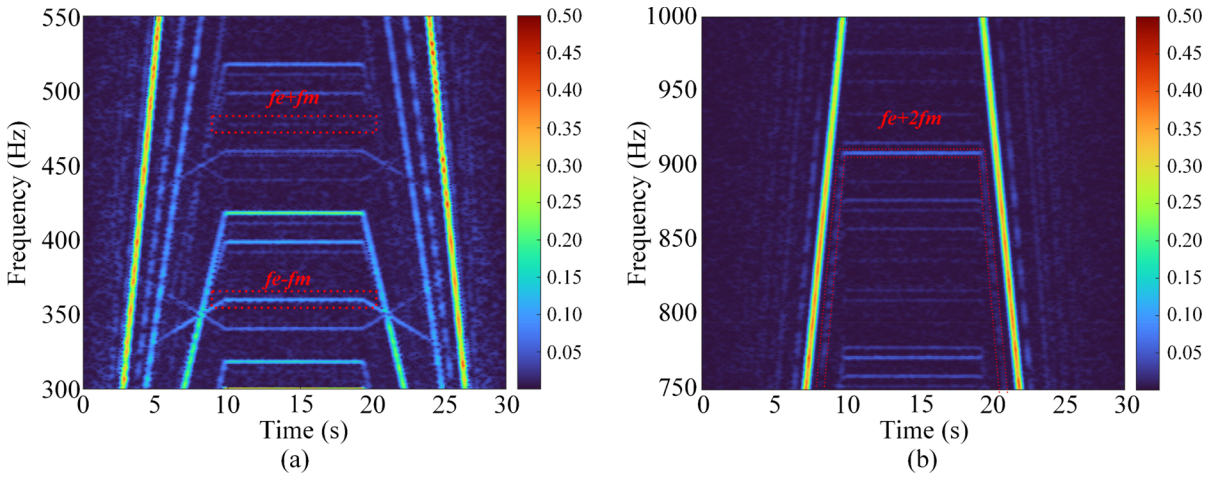

Fig. 25 Time–frequency refinement spectrum of dynamic response of electromechanical system under uniform speed condition. **a** 300–550 Hz refinement spectrum. **b** 750–1000 Hz refinement spectrum

Fourier transform (STFT) was employed to investigate the time–frequency domain characteristics of the system response. The results of the STFT analysis on the vibration acceleration and motor stator current signals in the electromechanical system under variable speed conditions are shown in Fig. 24a, b, respectively. In the STFT diagram of the vibration signal, the primary components include the meshing frequency f_m of the planetary drive system and its octave frequency. The behavior of the meshing frequency and rotational speed is consistent with the simulation results. Amplifying the frequency band of $f_m \pm f_c$, a frequency band near the meshing frequency is observed. The frequency bands in the test signal closely match those in the simulation signal, with a slight error attributed to the transmission error in the planetary drive system, well within the expected range. Comparing the STFT spectra of experimental data with simulation results, they are quite similar. The main distinction lies in the experimental signal, which includes significant field noise and various external interferences, resulting in the presence of clutter in the plot. In contrast, the simulation signal is cleaner and less affected by noise and disturbances. In the STFT diagram of the motor current, the power supply frequency f_e follows a pattern consistent with motor speed variations, and it dominates the STFT spectrum. It's important to note that the power supply frequency f_e is influenced by the meshing frequency f_m of the mechanical drive system. As a result, local amplification of the STFT spectrum reveals the presence of two frequency bands, $|f_m \pm f_e|$, which align with the results of the simulation analysis (Fig. 25).

5.2 Abrupt change in power supply frequency

Sudden changes in power supply frequency are common non-stationary conditions that can occur during motor operation. These abrupt shifts in power supply frequency often happen when the target speed of the motor control system is directly set to a specific value without the gradual acceleration and deceleration processes, resulting in an immediate change in the power supply frequency.

5.2.1 Simulation analysis results

To simulate this operating condition, we initiated the motor at an initial speed of 600 rpm for 2 s, and then suddenly changed the target speed to 1200 rpm at the 2-s mark. All other parameters and settings were maintained the same as in the previous sections. The resulting figures illustrate the EMCS's response to this sudden change in power supply frequency, displaying the electromagnetic torque, motor stator current, and gearbox vibration response, as shown in Fig. 26.

The dynamic changes in motor system speed, stator current, and electromagnetic torque depicted in Fig. 26 reveal the behavior of the system under the sudden increase in power supply frequency. At the

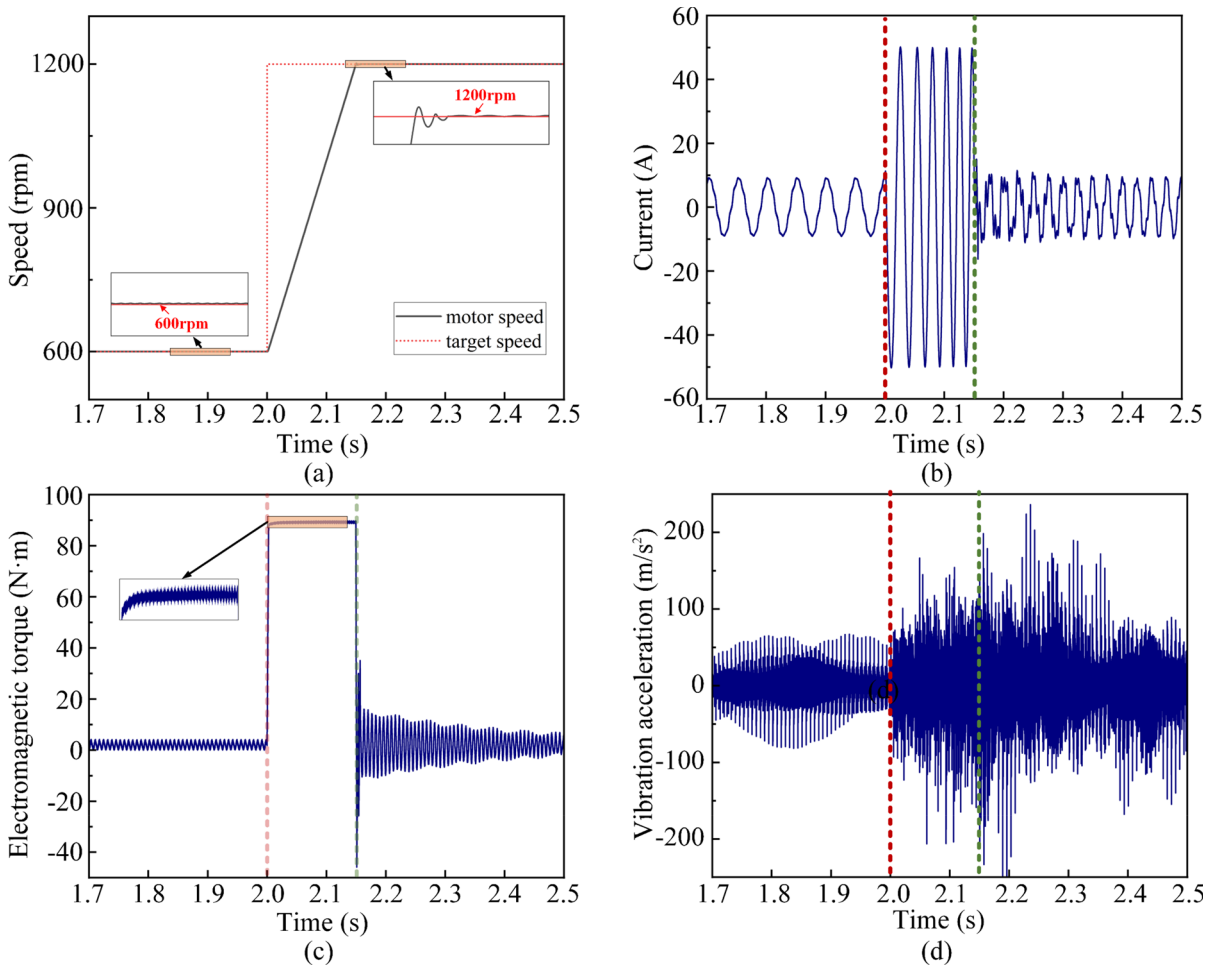

Fig. 26 Dynamic response of the electromechanical system to sudden power frequency surge. **a** Rotation speed. **b** Current. **c** Electromagnetic torque. **d** Vibration acceleration

outset of the power supply frequency surge, there is a substantial gap between the actual motor speed and the initial target speed, resulting in a sudden surge in the motor's stator current and electromagnetic torque, initiating motor acceleration. As shown in the figure, the acceleration process occurring from 2 to 2.15 s is akin to the uniform acceleration condition analyzed in the previous section. However, the distinction lies in the fact that the acceleration process is constrained by the motor's power and the control system's output limits. Even if the speed loop PI controller receives a substantial error input, its control output can only reach the maximum output value. This large error input saturates the controller, during which the torque current i_{sq} and electromagnetic torque T_e are predominantly determined by the electrical control system, resulting in less susceptibility to mechanical system vibration and smoother output. After 2.15 s, the rotational speed reaches a stable level, at which point, the electromagnetic torque experiences a significant reduction to achieve equilibrium with the load-side torque. Following this, the electromagnetic torque continues to oscillate briefly before reaching a stable state. The stator current exhibits a similar pattern, albeit with more noticeable fluctuations due to the increased mechanical system vibrations during this period.

It is important to note that the mechanical system's vibration acceleration follows a similar trend. During the initial 0–2 s of stable operation, the gearbox vibration acceleration maintains a relatively constant equilibrium position. However, when the power

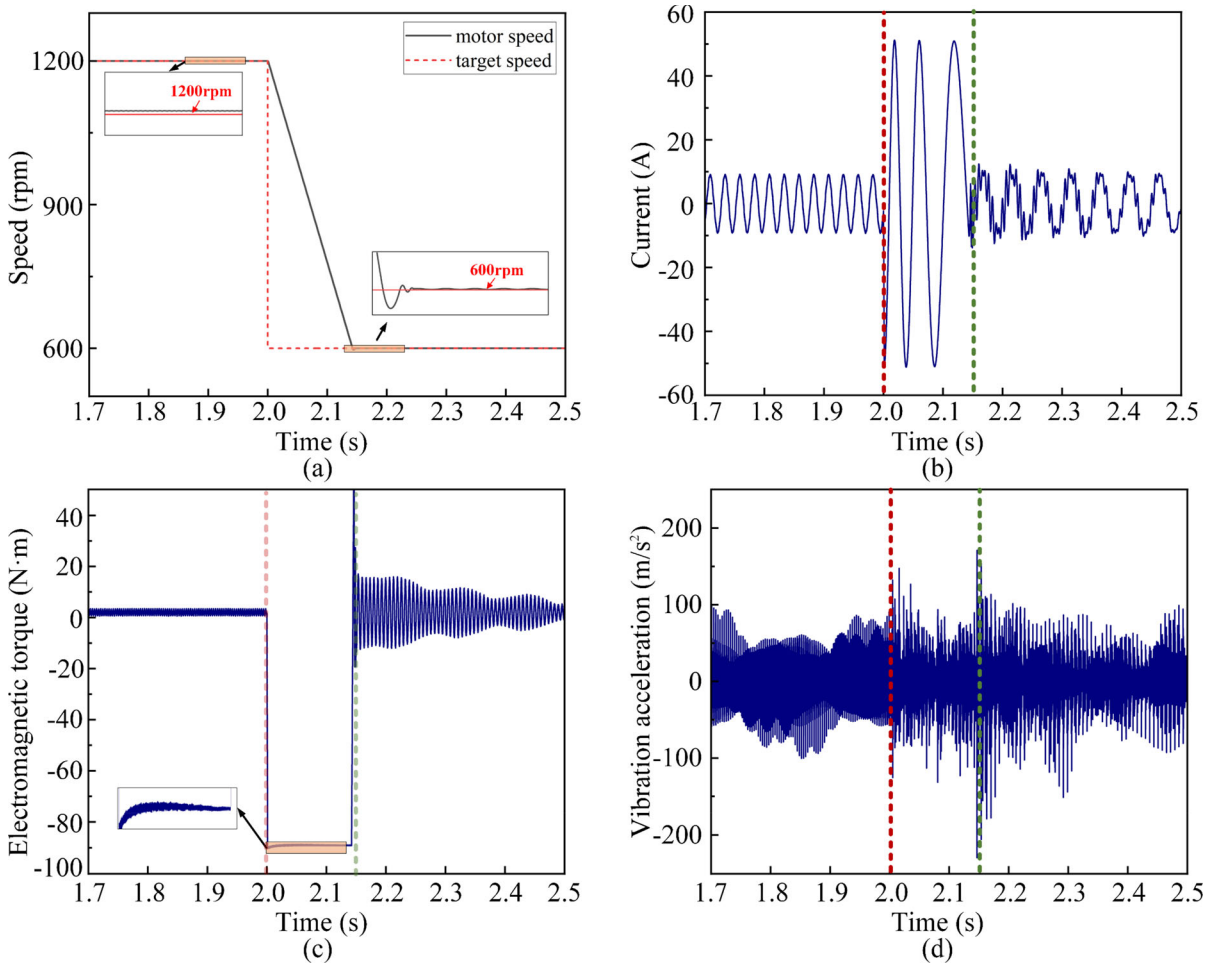

Fig. 27 Dynamic response of the electromechanical system to sudden power frequency drop. **a** Rotation speed. **b** Current. **c** Electromagnetic torque. **d** Vibration acceleration

supply frequency abruptly changes, the vibration amplitude increases significantly, and it oscillates briefly before returning to a stable state after the speed stabilizes.

The dynamic response of the motor-gear system under the condition of a power supply frequency drop is displayed in Fig. 27. The change in stator current and electromagnetic torque follows a pattern similar to that observed during a power supply frequency surge, but in the opposite direction. Therefore, we will not repeat here. Mechanical system vibration acceleration amplitude in the power supply frequency drop will enter the unstable state, then the vibration amplitude will tend to become smaller, and finally reach a stable state.

5.2.2 *Experimental analysis results*

To verify the simulation results of the EMCS under the sudden change of power supply frequency, relevant experiments were conducted on the experimental bench. In the experiments, the motor was initially running steadily at 600 rpm, and its speed was instantaneously increased from 600 to 1200 rpm in 2 s by adjusting the frequency converter. The time-domain waveforms of the motor current signals and the gearbox vibration signals during this sudden

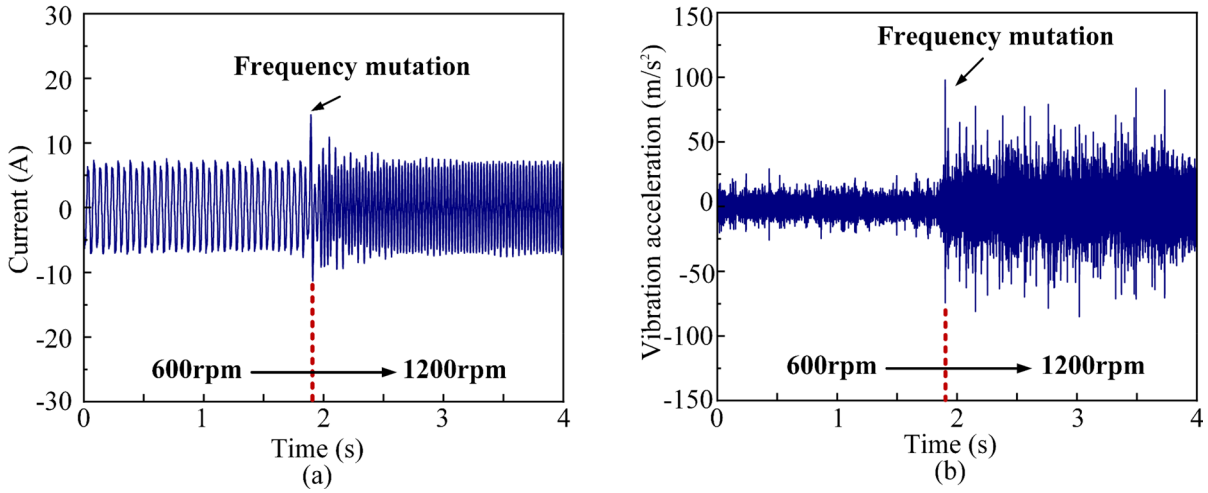

Fig. 28 Dynamic response of electromechanical system under power supply frequency surge condition (experimental results). **a** Current signal. **b** Vibration acceleration signal

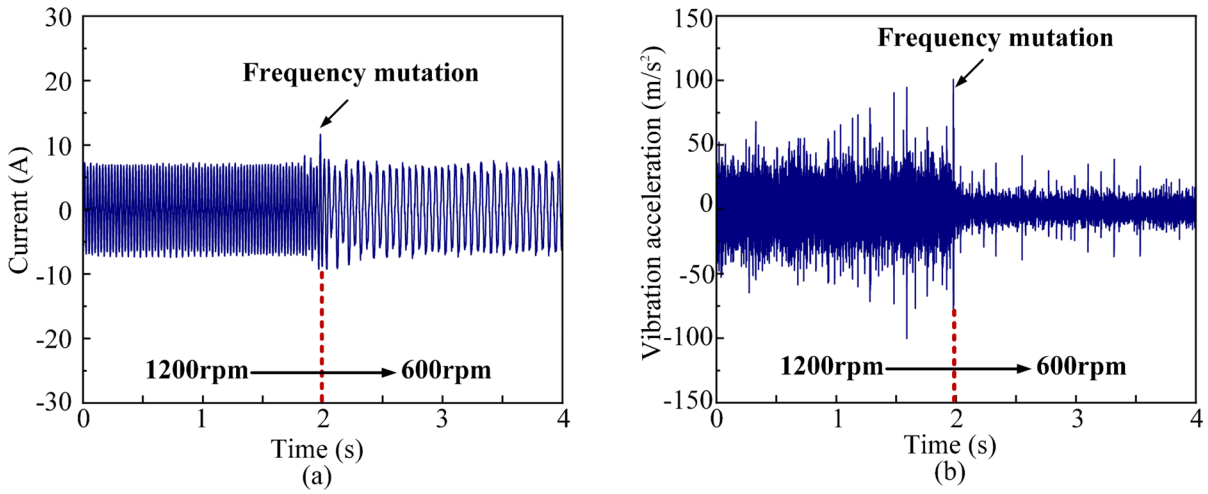

Fig. 29 Dynamic response of electromechanical system under sudden drop in power supply frequency condition (experimental results). **a** Current signal. **b** Vibration acceleration signal

increase in power supply frequency are shown in Fig. 28a, b, respectively. Similarly, in another set of experiments, the motor speed was set to decrease from 1200 to 600 rpm, and the time-domain waveforms of the motor current signal and gearbox vibration signal under the condition of a sudden drop in power frequency are displayed in Fig. 29a, b, respectively. These experimental results help validate the simulation findings.

Consistent with the results of the simulation analysis, in the conditions of a sudden increase in power supply frequency, there is a significant initial gap between the actual speed of the motor and the target speed. During this time, the motor stator current experiences a sudden increase, driving the motor to accelerate. The current and electromagnetic torque are primarily determined by the electrical control system at this point. Subsequently, as the speed reaches a stable level, the current experiences a substantial decrease and continues to oscillate for a brief period until it reaches a stable state. The amplitude of mechanical system vibration acceleration follows a similar pattern, with a significant impact during the sudden change in motor frequency, followed by

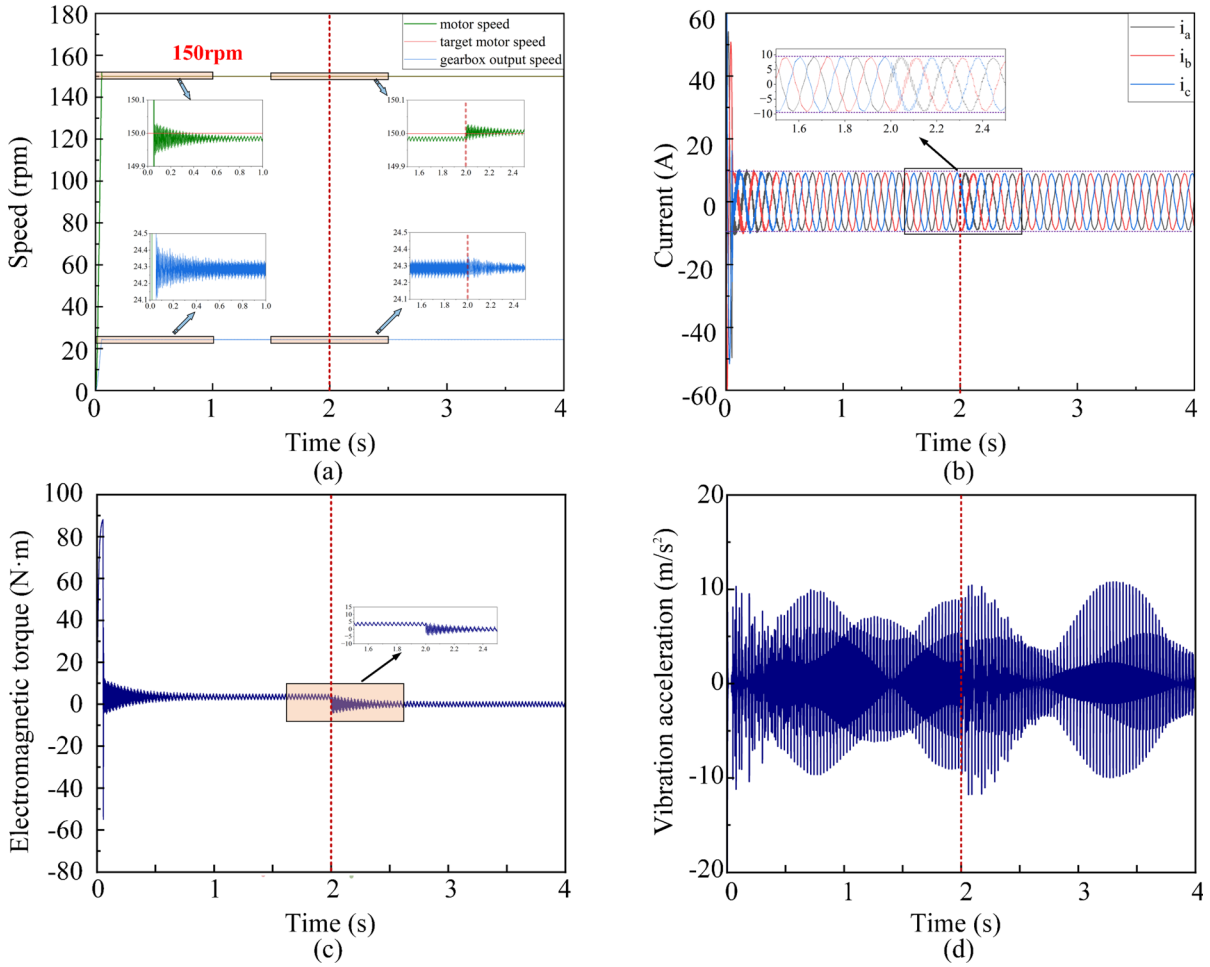

Fig. 30 Dynamic response of electromechanical system under sudden load change condition (simulation). **a** Rotation speed. **b** Current. **c** Electromagnetic torque. **d** Vibration acceleration

fluctuations and an eventual decrease in amplitude. Under the conditions of a sudden drop in power supply frequency, the motor stator current also experiences a sudden increase, and during this period, the current and electromagnetic torque are mainly determined by the electrical control system. As the speed reaches a stable level, the current exhibits a significant decrease and continues to oscillate for a short period before reaching a stable state. Mechanical system vibration acceleration amplitude is significantly affected initially, followed by stable fluctuations and an increase in amplitude. The experimental results are consistent with the patterns observed in the simulation analysis.

5.3 Abrupt load change conditions

Motor-gear transmission systems often operate in demanding environments, where sudden changes in load are common. Therefore, it is crucial to investigate the electrical characteristics and dynamic responses of PMCS under sudden load changes. To simulate the effects of sudden load changes on the dynamic characteristics of the motor-gear system, we used Simulink to set up a step load change in a simulation process. The motor's steady speed was set to 150 rpm, with a load of 20 N·m. At 2 s, there was a sudden load change to 0. The simulation duration was 4 s. Under these conditions, we observed the motor's rotational speed, the planetary shaft's output rotational speed, the electromagnetic torque of the EMCS, the stator

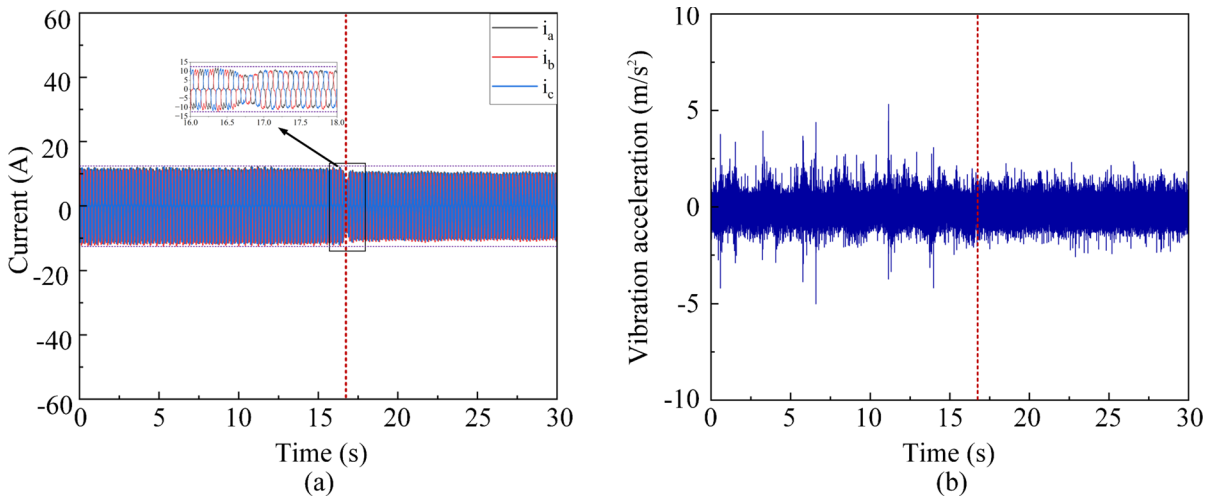

Fig. 31 Dynamic response of electromechanical system under sudden load change operating conditions (test). **a** Current signal. **b** Vibration acceleration signal

current of the motor, and the vibration response of the gearbox, as shown in Fig. 30.

To validate the accuracy of the simulation and analysis results for the electromechanical system under sudden load conditions, an experimental test of the electromechanical system was conducted. The motor was set to a stable speed of 150 rpm, and the load applied by the magnetic powder brake was adjusted by controlling the current with the tension controller. During the experiment, instant loading and unloading were achieved by opening and closing the tension controller switch. All other experimental settings were consistent with the simulation conditions, and the entire experimental process lasted for 4 s. At the start of the experiment, when the motor speed and the load were stabilized at 150 rpm and 20 N·m, respectively, the tension controller switch was closed to achieve instantaneous unloading within 2 s. The magnetic particle brake was loaded and unloaded instantly during this sudden change of load. The motor current and gearbox vibration acceleration signals obtained through the experiment under these sudden load changes are shown in Fig. 31.

The simulation and experimental analysis reveal that when the load is suddenly reduced to zero, the load torque acting on the motor shaft experiences a rapid drop. This sudden change causes the actual motor speed to fluctuate, initially surpassing the target speed. In response, the PI controller adjusts its output to bring the motor speed back into proximity to the target speed, overcoming the impact of the substantial deviation. The motor speed then gradually stabilizes near the target speed. Simultaneously, the motor's electromagnetic torque decreases to reach an equilibrium with the reduced load torque, and the oscillations tend to stabilize. The change in current follows a similar pattern. Because the mechanical load is abruptly set to zero, the motor reduces the current to balance the external load and maintain its original speed.

In the previous section, we discussed the effects of relatively small loads, with the highest setting being only 20 N-m, on the current and vibration signals, which showed relatively weak impacts. To further explore the consequences of heavy load conditions and sudden load changes on the dynamic behavior of the planetary drive's EMCS, we conducted a sudden load test using an industrial-grade 55 kW planetary drive test bench, as depicted in Fig. 32. This test bench comprises several essential components, including a drive motor, a load motor, speed and torque sensors, a test gearbox, an incremental speed gearbox, a frequency converter, a control cabinet, a signal acquisition system, and other equipment. The drive motor powers the test gearbox by rotating it, and the load motor, controlled by adjusting the excitation current, acts as the load applied to the test gearbox. This setup allows precise control of the torque on the gearbox, enabling simulations of different loading conditions. The signal acquisition system is equipped with Hall

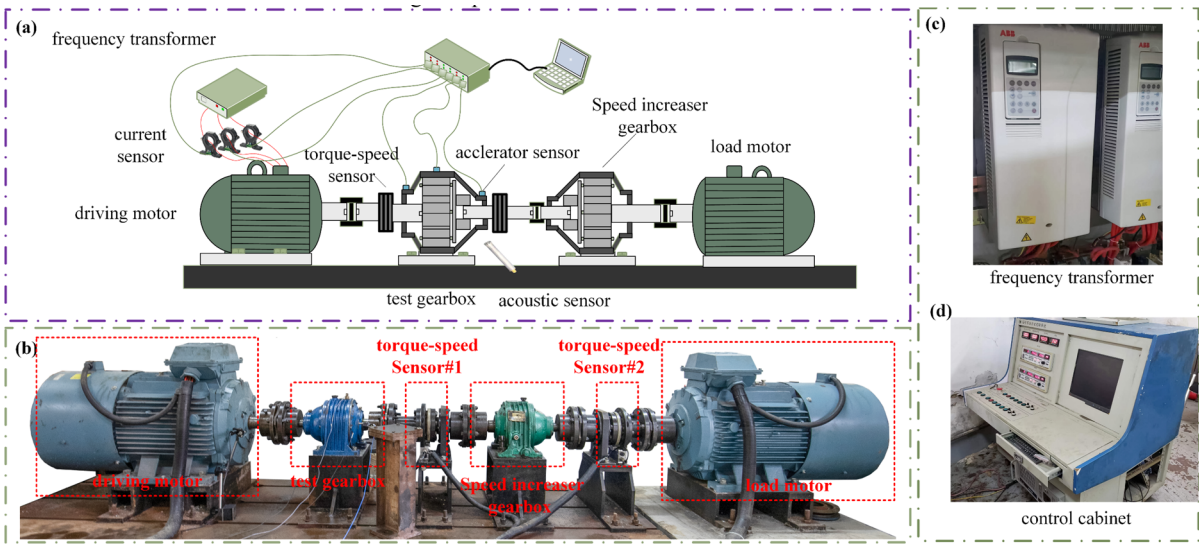

Fig. 32 Large-scale industrial-level "back-to-back" planetary drive failure simulation test bench. **a** Schematic diagram of the test bench. **b** Experimental test site. **c** Frequency converter. **d** Control cabinet

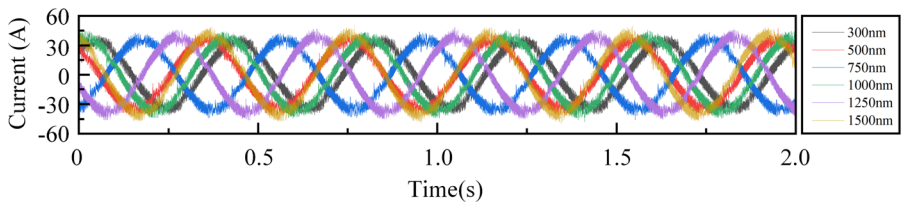

Fig. 33 Time domain waveforms of motor current under different load conditions

current sensors, B&K vibration acceleration sensors, an NI-9231 data acquisition card, a laptop computer, and test software. The Hall current sensors are positioned between the inverter and the drive motor to capture three-phase current signals from the motor. Meanwhile, the three vibration acceleration sensors are strategically placed at the input shaft, output shaft, and the upper end of the toothed ring of the test gearbox. These sensors simultaneously collect data during the operation of the gearbox. The sampling rate for all channels is set to 12,800 Hz, and the data is collected over a period of 28 s. This advanced setup allows for an in-depth exploration of the dynamic responses of the EMCS under varying load and sudden load conditions using a large-scale 55 kW industrial-grade planetary drive test bench.

The test was initially conducted on the test rig at a constant speed of 150 rpm, and the load on the motor was varied by adjusting the magnitude of the excitation current applied to the loaded motor. The test began with an initial load of 300 N·m and then increased the load incrementally. Vibration and current signals were collected under working conditions of 500 N·m, 750 N·m, 1000 N·m, 1250 N·m, and 1500 N·m. The dynamic characteristics of the EMCS were analyzed based on the time domain and the motor's spectrum under different load conditions. The time-domain waveforms of the motor current under these various load conditions are depicted in Fig. 33. It can be challenging to discern changes in current amplitude from these time-domain waveforms. To provide a more comprehensive analysis, various time-domain indices, including the peak-to-peak value, RMS value, crest factor, pulse factor, and margin factor of the current signals under different loads, were calculated and are displayed in Fig. 34. As seen in Fig. 34, as the load increases, the motor current's peak value and RMS value also increase, while the crest factor, pulse factor, and margin factor decrease. This observed phenomenon aligns with the simulation results,

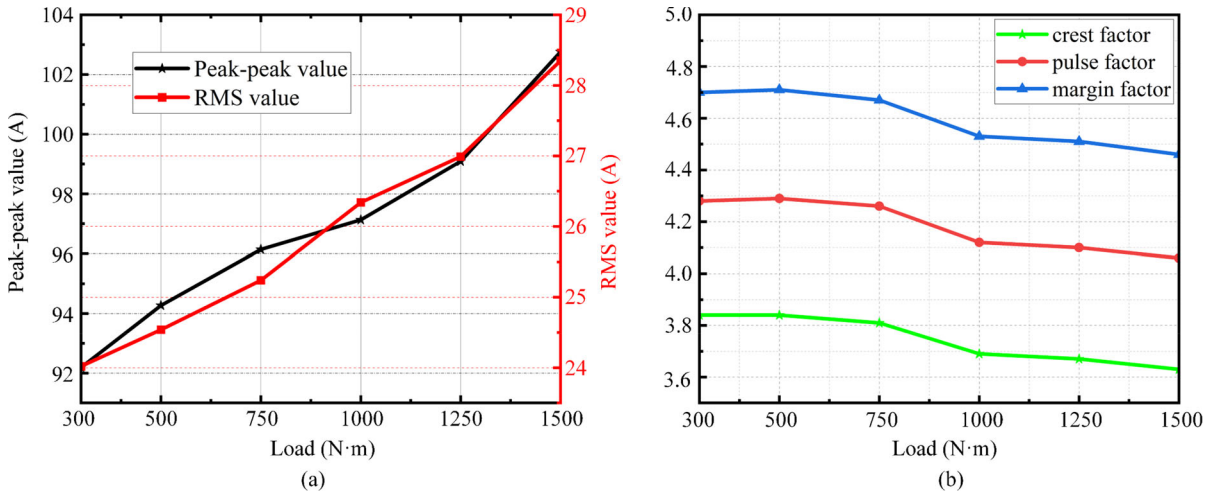

Fig. 34 Time domain index of motor current under different load conditions. **a** Dimensioned indicator. **b** None dimension indicator

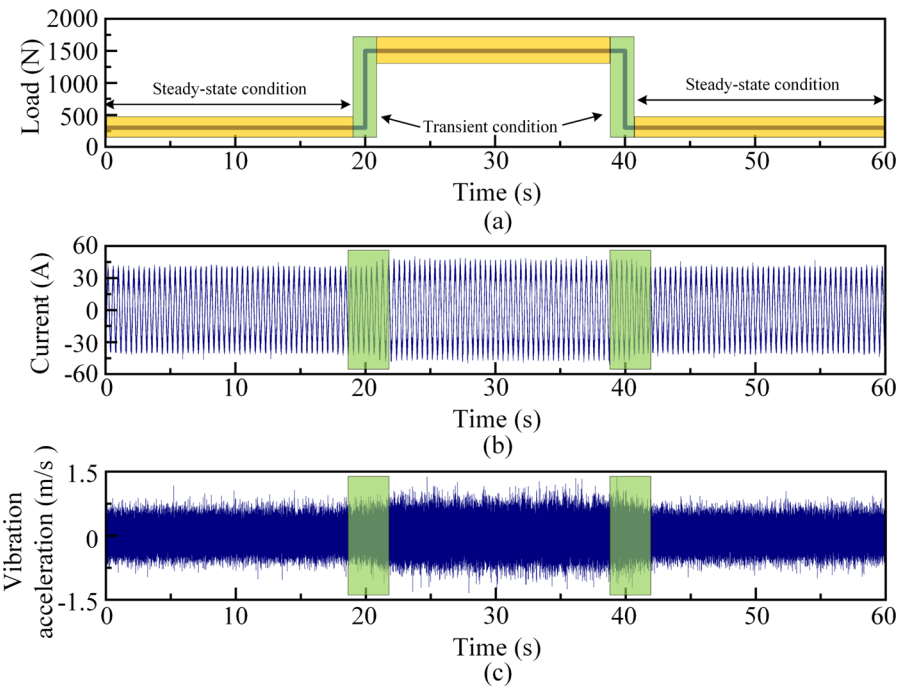

Fig. 35 Current and vibration response of electromechanical system under sudden load change condition. **a** Load variation curve. **b** Current signal. c Vibration acceleration signal

indicating the expected changes in the motor's dynamic response under varying load conditions.

The experiment continued by investigating the dynamic characteristics of the electromechanical system under sudden changes in load conditions on the test bench. The entire experimental process lasted for 60 s. Initially, the load was set at 300 N·m for the first 20 s. At the 20-s mark, the load was abruptly changed to 1500 N·m by controlling the load motor. After running stably for 20 s at 1500 N·m, the load was suddenly changed back to 300 N·m. The load change trend throughout the entire experimental process is displayed in Fig. 35a. The motor current and vibration acceleration of the planetary gearbox collected during this test are presented in Fig. 35b, c. Their time-domain waveform trends align with the changes in the load, demonstrating sensitivity to load variations. Short-time Fourier transformations (STFT) were

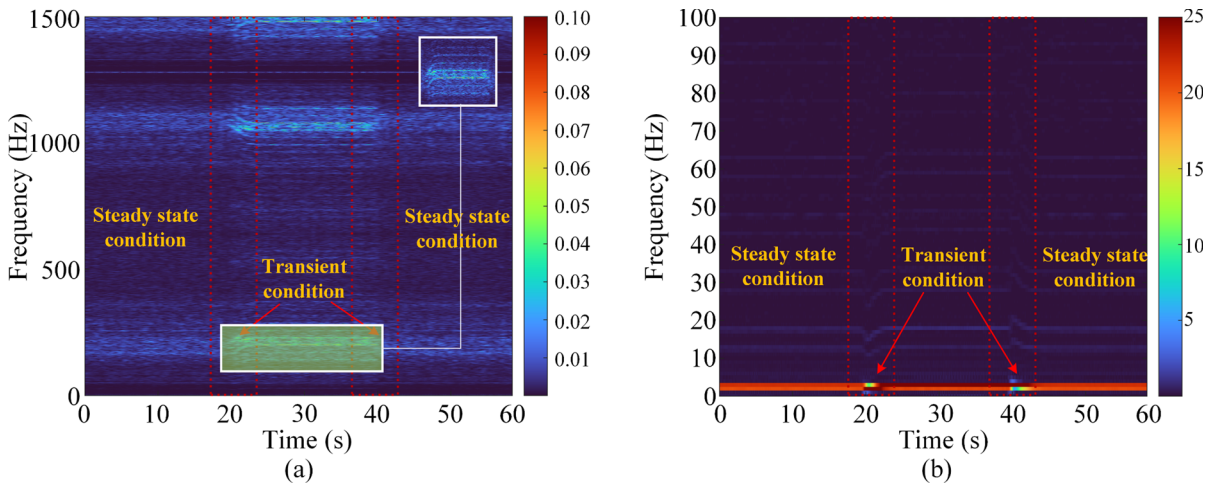

Fig. 36 STFT spectra of motor current and gear vibration signals under sudden load change conditions. **a** Vibration signal STFT spectrum. **b** Current signal STFT spectrum

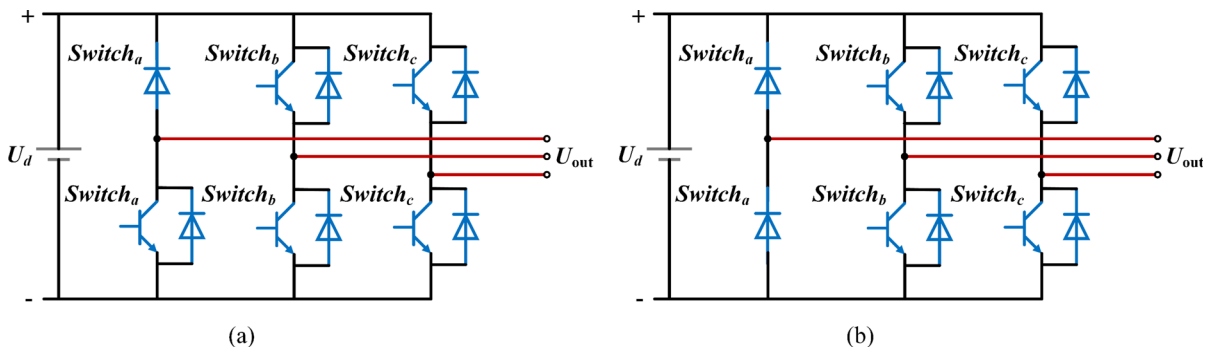

Fig. 37 Schematic diagram of the inverter power supply in non-ideal state. **a** Single-switch open-circuit state. **b** Unidirectional bridge arm open state

applied to the vibration acceleration and current signals, resulting in the spectra shown in Fig. 36a, b, respectively.

In the STFT spectra of both signals, it is evident that the sudden changes in load do not significantly affect the spectral distribution. The main frequency component of the planetary gearbox's vibration acceleration during sudden load changes remains f_m. Notably, there is a larger response amplitude in the vibration acceleration, and the frequency component is more pronounced during the moments of load changes. Similarly, the STFT spectrum of the motor current continues to be dominated by $|f_m \pm f_e|$, with more prominent color changes in the frequency band observed during sudden load change periods. This experimental evidence supports the conclusion that sudden load changes induce more pronounced dynamic responses in the electromechanical system, consistent with the simulation results.

6 Dynamic characteristics of PMCS under non-ideal conditions

In this section, we investigate the dynamic characteristics of the electromechanical coupling model for the three-phase inverter power switching elements under non-ideal states. Specifically, we focus on two open-

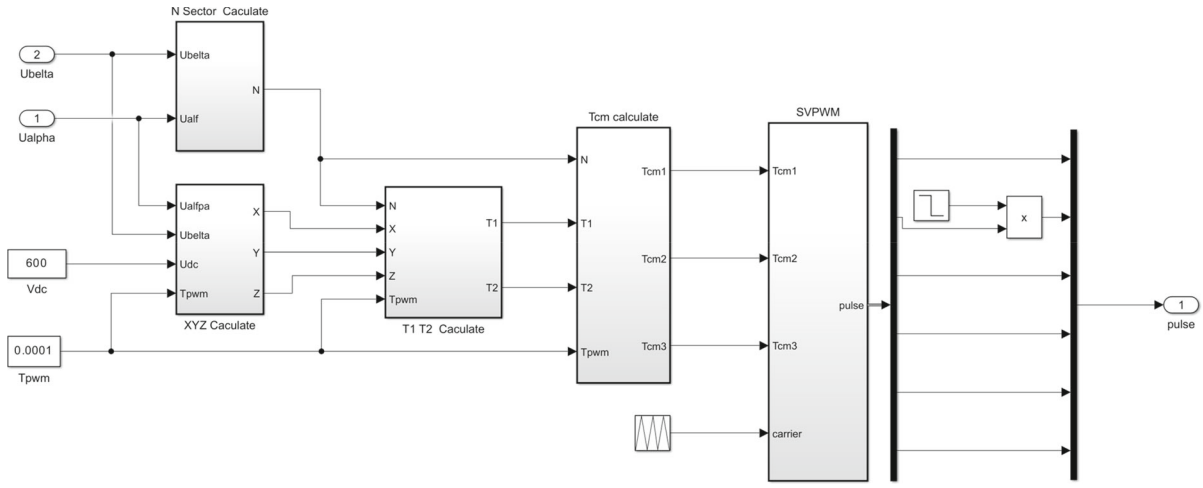

Fig. 38 Schematic of Simulink single switching tube open circuit setup

circuit states of the inverter: the open-circuit state of a single switching tube in the inverter bridge and the open-circuit state of a unidirectional bridge arm. The schematic diagram of the inverter under non-ideal conditions is illustrated in Fig. 37, which includes the inverter DC power supply and six power switching elements. This analysis aims to reveal the mapping relationship between the motor stator current and the dynamic response of the planetary drive system when the inverter's power switching elements are in these non-ideal states.

6.1 Single-switch open-circuit state

In order to simulate the open-circuit state of a single switching tube in the inverter, the final output switch signal is manipulated in the SVPWM module within Simulink. The output value of this signal is maintained at zero after 1 s, effectively simulating the open-circuit condition in phase a. The schematic for simulating this single switch open-circuit state in Simulink is shown in Fig. 38. The simulation settings include a target motor speed of 1200 rpm, disconnecting the single switching tube in phase a after 1 s when the speed stabilizes, and ending the simulation after 3 s. The gear train operates under a partial load of 12 N·m. The results of this simulation include motor speed, stator current, electromagnetic torque, and vibration response of the planetary gear under the open state of the single switching tube, which are depicted in Fig. 39.

The observations from Fig. 39 reveal that when a single switching tube in the inverter power supply is in an open-circuit state, various aspects of the system, including the motor's rotational speed, stator current, electromagnetic torque, and gearbox vibration response, exhibit abnormal behavior. The motor's actual speed oscillates back and forth regularly near the target speed. The electromagnetic torque experiences a significant and sudden change at the moment of the switching tube opening, followed by regular oscillations. These waveform behaviors occur because, in the absence of a functioning switching tube, the inverter power supply cannot output control signals as usual. However, the internal magnetic chain calculations, SVPWM sector judgment, and other aspects of the directional control system remain in a normal state. The motor's output signal is regulated by the system's feedback, resulting in the observed regular fluctuations. The changes in the gearbox's vibration response exhibit a similar pattern, with a rapid increase in instantaneous amplitude during the open-circuit state, followed by regular fluctuations. These vibration response fluctuations are closely related to the fluctuations in speed and electromagnetic torque.

In the case of a single switching tube in the inverter power supply being in an open-circuit state, the motor's a-phase winding is only connected to the bus voltage terminal through the continuity diode. As a result, the a-phase current will only appear in the positive half-wave and is nearly zero in the negative

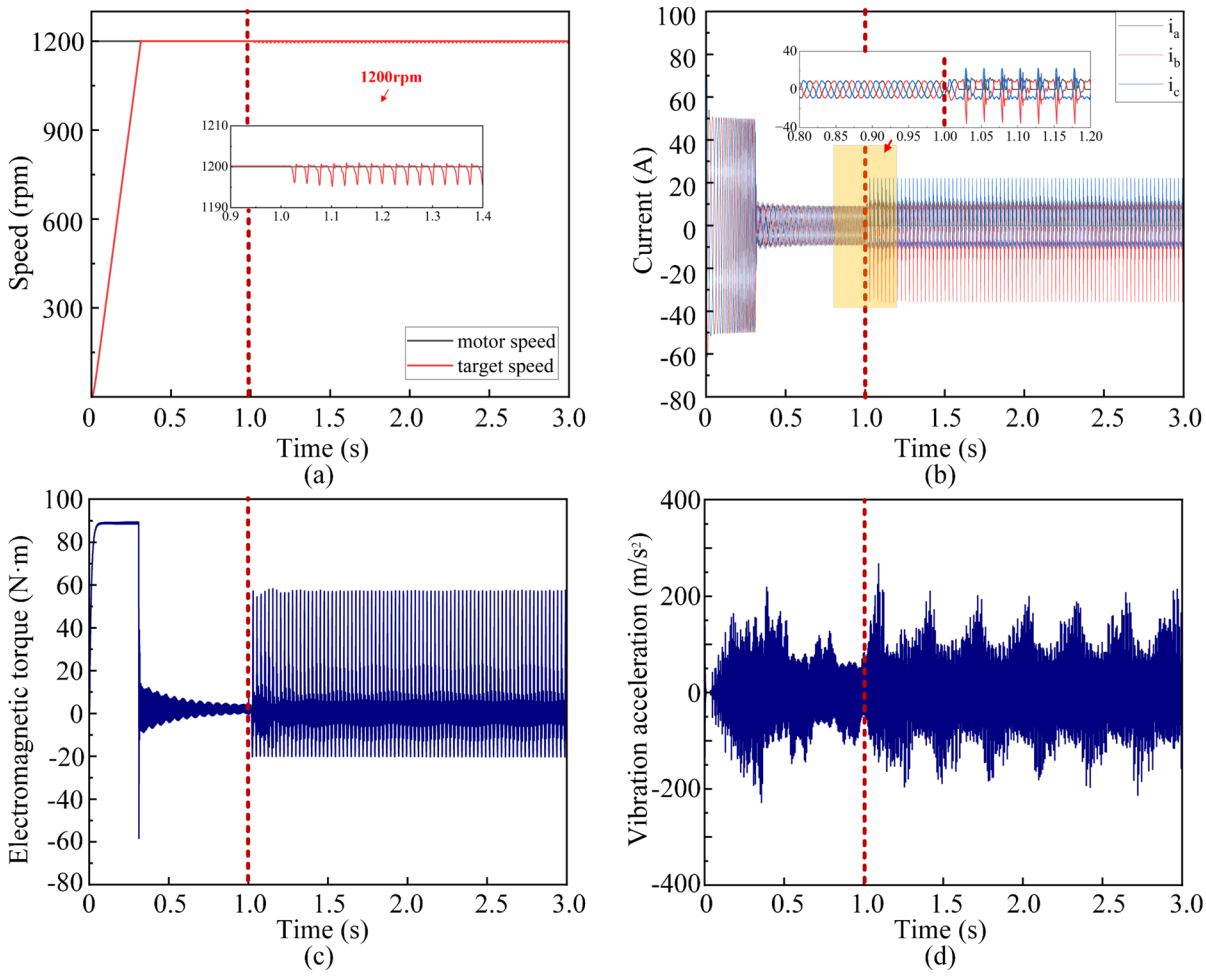

Fig. 39 Dynamic response of the electromechanical system in the open state of the single switching tube. **a** Rotation speed. **b** Current. **c** Electromagnetic torque. **d** Vibration acceleration

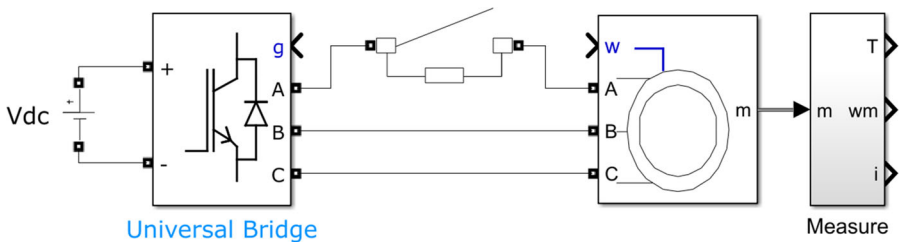

Fig. 40 Schematic of Simulink setup for unidirectional bridge arm open circuit

half-cycle. This situation causes a sudden increase in the amplitude of the remaining current flowing through the rest of the inverter switching tubes. As observed in Fig. 39b, the amplitudes of the currents flowing through the b and c phases are close to the startup current. Prolonged operation in this state could lead to the burning of other switching tubes in the inverter power supply. The asymmetry in the three-phase current due to this situation leads to several undesirable consequences, for example, motor output torque jitter, speed instability, increased mechanical equipment vibration. These effects highlight the critical importance of maintaining the proper functioning of the inverter power supply components for

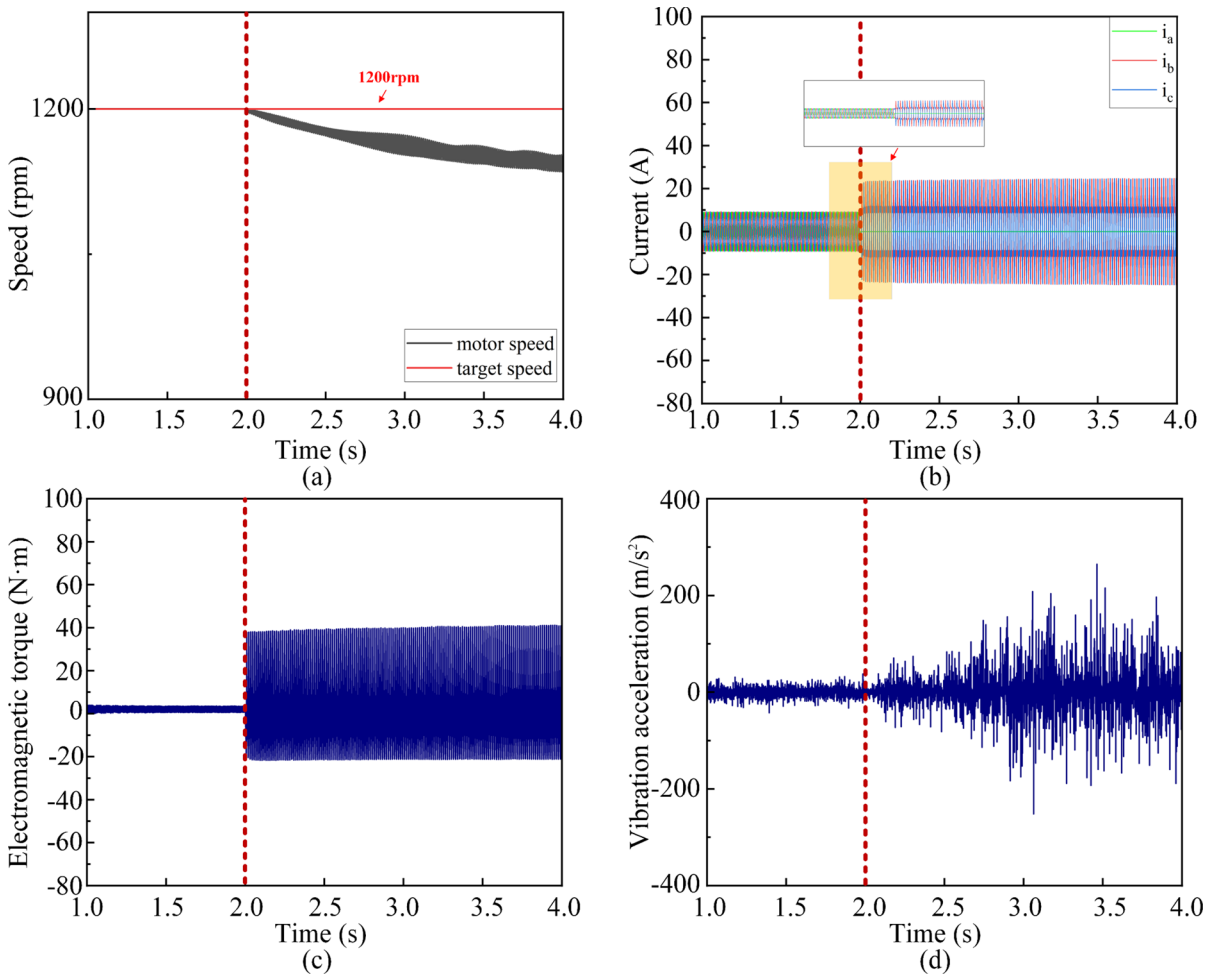

Fig. 41 dynamic response of electromechanical system under unidirectional bridge arm open circuit condition. **a** Rotation speed. **b** Current. **c** Electromagnetic torque. **d** Vibration acceleration

the stability and reliability of the electromechanical system.

6.2 Unidirectional bridge arm open state

When both switching tubes in the three-phase inverter power supply are in an open-circuit state, the entire unidirectional bridge arm becomes open-circuited, essentially taking the motor out of phase, as illustrated in Fig. 37b. To simulate this open-circuit state of the unidirectional bridge arm, we configured the circuit breaker in the middle of the a-phase power supply. The simulation settings in Simulink are shown in Fig. 40. The simulation begins with the motor starting and operating stably at 1200 rpm, disconnects the a-phase circuit at 2 s, and concludes after 4 s. The gear train load remains at 12 N·m throughout the simulation. The extracted data includes motor speed, stator current, electromagnetic torque, and planetary gear vibration response under the condition of phase absence, as shown in Fig. 41.

As depicted in Fig. 41, it is evident that the motor-gear coupling system experiences a substantial speed reduction and instability when the motor lacks one phase. The motor's a-phase current undergoes an abrupt transition from a stable state to zero, causing significant changes and an increase in amplitude in the b-phase and c-phase current waveforms. This abrupt current shift is accompanied by an immediate increase in electromagnetic torque. Additionally, the amplitude of gearbox vibration acceleration rises noticeably

when the motor operates with a missing phase and remains unstable after 2 s.

This behavior can be primarily attributed to the inverter's inability to provide normal control signals due to the open circuit in one of the bridge arms, resulting in a significant deviation in the output signal. This, in turn, leads to a gradual reduction in the feedback regulation effect and a continuous decline in motor speed, rendering it unable to attain the desired speed. Furthermore, when one of the three-phase power supplies is disconnected, it generates a substantial braking torque due to the reversed magnetic field sequence, thereby reducing the motor's output torque. With the load remaining constant, this leads to an increase in the rotational speed and significantly higher current flowing through the stator winding compared to normal operation. As a consequence, there is an increase in copper and iron consumption, which can elevate motor temperature and potentially damage the stator winding. Therefore, it is essential to develop corresponding relay protection schemes in response to such scenarios. These results also offer valuable theoretical guidance for the condition monitoring of PMCS.

7 Conclusions

In this study, we thoroughly considered various internal and external excitation factors such as time-varying meshing stiffness, bearing support stiffness, and meshing errors under variable speed conditions. Firstly, we established a mechanical model for planetary gear systems suitable for analyzing non-steady state conditions, including uniform speed, sudden changes in speed, abrupt load changes, and more. Subsequently, we constructed an equivalent circuit model for a three-phase asynchronous motor based on rotor magnetic flux orientation control and space vector modulation algorithms. By establishing the coupling relationship between the electrical and mechanical components of the motor drive system, we created a complete electromechanical system coupling model suitable for analyzing non-steady-state conditions, including time-varying speed, variable loads, sudden frequency changes, and non-ideal conditions such as voltage spikes and current phase loss. The discussions on electromechanical coupling effects yielded the following specific conclusions:

(1) In a stable speed operation of the EMCS, it was found through a combined analysis of simulation and experimental results that the motor current signal is modulated by the planetary gear transmission system's meshing frequency. The spectrum primarily comprises the power supply frequency f_e and the combination frequencies of the power supply frequency and meshing frequency $|f_e \pm nf_m|$, with the power supply frequency f_e dominating. High-frequency components and related frequencies are less distinct, primarily due to the significant rotor inertia of the motor and the inductance produced by the stator winding, making the motor system less sensitive to high-frequency excitation and exhibiting low-pass filter characteristics.

(2) A comprehensive study of the dynamic characteristics of the gear-motor coupling system under various non-steady state conditions was carried out, analyzing the variations in electromagnetic torque, stator current, and gear vibration responses under different conditions such as uniform speed, sudden changes in power supply frequency, and abrupt load changes. The faithful mapping relationships between mechanical vibration, motor stator current, and electromagnetic torque were revealed in the time domain, frequency domain, and time–frequency domain for different conditions. Compared to traditional direct motor control models, the proposed model more accurately reflects the system's transient dynamic characteristics. When designing and selecting motor-gear systems, it is crucial to consider the coupling effects between the carrier frequency of the electrical part and the meshing frequency of the mechanical part to avoid resonance issues caused by close harmonic frequencies.

(3) Further exploration of the dynamic characteristics of the gear-motor coupling system under non-ideal states of the asynchronous motor's electrical system. When a single switching tube in the inverter power supply is open-circuited, the system experiences motor speed instability, torque fluctuations, and significant mechanical equipment vibration amplitudes due to the asymmetry in three-phase currents. When a unidirectional bridge arm in the inverter power supply is open-circuited, the a-phase current

drops to zero, causing the motor's speed to rapidly decrease, leading to potential overheating and damage to the stator winding due to increased current and copper and iron consumption. These findings provide theoretical guidance for overall condition monitoring of electromechanical systems.

Acknowledgements This research work is supported by the National Key Research and Development Program of China (Grant No. 2019YFB2004600) and the Fundamental Research Funds for the Central Universities (Grant No. DUT22LAB508).

Funding The funding was provided by the National Key Research and Development Program of China (Grant No. 2019YFB2004600) and the Fundamental Research Funds for the Central Universities (Grant No. DUT22LAB508).

Data availability Data availability Data used to support findings of this study are included within the article.

Declarations

Conflict of interest The all authors declare that they have no known competing financial interests or personal relationships that could have appeared to influence the work reported in this paper.

References

1. Zhang, C., Wei, J., Liu, H., Zhang, X.: Similarity and vibration signal prediction of planetary gear transmission system based on hierarchy analysis. Appl. Math. Model. **123**, 856–870 (2023)
2. Han, Q., Wang, T., Ding, Z., Xu, X., Chu, F.: magnetic equivalent modeling of stator currents for localized fault detection of planetary gearboxes coupled to electric motors. IEEE Trans. Industr. Electron. **68**(3), 2575–2586 (2021)
3. Kahraman, A.: Planetary gear train dynamics. ASME J. Mech. Des. **116**(3), 714–720 (1994)
4. Parker, R.G., Lin, J.: Mesh phasing relationships in planetary and epicyclic gears. J. Mech. Des. **126**(2), 365–370 (2004)
5. Guo, Y., Parker, R.G.: Dynamic modeling and analysis of a spur planetary gear involving tooth wedging and bearing clearance nonlinearity. Eur. J. Mech. A. Solids **29**(6), 1022–1033 (2010)
6. Kim, W., Lee, J.Y., Chung, J.: Dynamic analysis for a planetary gear with time-varying pressure angles and contact ratios. J. Sound Vib. **331**(4), 883–901 (2012)
7. Xiao, Z., Zhou, C., Chen, S., Li, Z.: Effects of oil film stiffness and damping on spur gear dynamics. Nonlinear Dyn. **96**(1), 145–159 (2019)
8. Shi, J.-F., Gou, X.-F., Zhu, L.-Y.: Five-state engaging model and dynamics of gear-rotor-bearing system based on time-varying contact analysis considering gear temperature and lubrication. Appl. Math. Model. **112**, 47–77 (2022)
9. Zhang, K., Li, H., Cao, S., Wang, C., Sun, B., Liu, A.: Investigation on planetary gearbox fault mechanism under variable speed conditions based on rigid-flexible coupling dynamics model. Eng. Fail. Anal. **133**, 105994 (2022)
10. Yang, X., Lei, Y., Liu, H., Yang, B., Li, X., Li, N.: Rigid-flexible coupled modeling of compound multistage gear system considering flexibility of shaft and gear elastic deformation. Mech. Syst. Signal Process. **200**, 110632 (2023)
11. Wang, P., Xu, H., Ma, H., Han, H., Yang, Y.: Effects of three types of bearing misalignments on dynamic characteristics of planetary gear set-rotor system. Mech. Syst. Signal Process. **169**, 108736 (2022)
12. Liang, X., Zuo, M.J., Pandey, M.: Analytically evaluating the influence of crack on the mesh stiffness of a planetary gear set. Mech. Mach. Theory **76**, 20–38 (2014)
13. Jiang, F., Ding, K., He, G., Sun, Y., Wang, L.: Vibration fault features of planetary gear train with cracks under time-varying flexible transfer functions. Mech. Mach. Theory **158**, 104237 (2021)
14. Liu, X., Fan, Z., Cao, Z., Liu, Y., Kang, Z., Hu, Y.: Fault signal simulation and service condition monitoring of cracked gear system. IEEE Trans. Instrum. Meas. **72**, 1–14 (2023)
15. Liang, X., Zuo, M.J., Patel, T.H.: Evaluating the time-varying mesh stiffness of a planetary gear set using the potential energy method. Proc. Inst. Mech. Eng. C J. Mech. Eng. Sci. **228**(3), 535–547 (2013)
16. Feki, N., Clerc, G., Velex, P.: An integrated electro-mechanical model of motor-gear units—applications to tooth fault detection by electric measurements. Mech. Syst. Signal Process. **29**, 377–390 (2012)
17. Ottewill, J.R., Ruszczyk, A., Broda, D.: Monitoring tooth profile faults in epicyclic gearboxes using synchronously averaged motor currents: Mathematical modeling and experimental validation. Mech. Syst. Signal Process. **84**, 78–99 (2017)
18. Feng, Z., Chen, X., Zuo, M.J.: Induction motor stator current AM-FM model and demodulation analysis for planetary gearbox fault diagnosis. IEEE Trans. Industr. Inf. **15**(4), 2386–2394 (2019)
19. Chen, X., Feng, Z.: Induction motor stator current analysis for planetary gearbox fault diagnosis under time-varying speed conditions. Mech. Syst. Signal Process. **140**, 106691 (2020)
20. Touti, W., Salah, M., Bacha, K., Chaari, A.: Condition monitoring of a wind turbine drivetrain based on generator stator current processing. ISA Trans. **128**(Pt A), 650–664 (2022)
21. Zhang, K., Li, H., Cao, S., Yang, C., Sun, F., Wang, Z.: Motor current signal analysis using hypergraph neural networks for fault diagnosis of electromechanical system. Measurement **201**, 111697 (2022)
22. Zhang, K., Li, H., Cao, S., Lv, S., Yang, C., Xiang, W.: Trusted multi-source information fusion for fault diagnosis of electromechanical system with modified graph convolution network. Adv. Eng. Informat. **57**, 102088 (2023)
23. Liu, C., Qin, D., Lim, T.C., Liao, Y.: Dynamic characteristics of the herringbone planetary gear set during the

variable speed process. J. Sound Vib. **333**(24), 6498–6515 (2014)
24. Bai, W., Qin, D., Wang, Y., Lim, T.C.: Dynamic characteristics of motor-gear system under load saltations and voltage transients. Mech. Syst. Signal Process. **100**, 1–16 (2018)
25. Yi, Y., Qin, D., Liu, C.: Investigation of electromechanical coupling vibration characteristics of an electric drive multistage gear system. Mech. Mach. Theory **121**, 446–459 (2018)
26. Xu, X., Han, Q., Qin, Z., Chu, F.: Analytical methods for the radial electromagnetic vibration of stator in permanent magnet motors with an amorphous alloy core. Mech. Syst. Signal Process. **145**, 106909 (2020)
27. Shu, R., Wei, J., Tan, R., Wu, X., Fu, B.: Investigation of dynamic and synchronization properties of a multi-motor driving system: theoretical analysis and experiment. Mech. Syst. Signal Process. **153**, 107496 (2021)
28. Yousfi, B.E., Soualhi, A., Medjaher, K., Guillet, F.: Electromechanical modeling of a motor–gearbox system for local gear tooth faults detection. Mech. Syst. Signal Process. **166**, 108435 (2022)
29. Chen, R., Qin, D., Liu, C.: Dynamic modelling and dynamic characteristics of wind turbine transmission gearbox-generator system electromechanical-rigid-flexible coupling. Alex. Eng. J. **65**, 307–325 (2023)
30. Xie, C., Shu, X.: A new mesh stiffness model for modified spur gears with coupling tooth and body flexibility effects. Appl. Math. Model. **91**, 1194–1210 (2021)
31. Wan, Z., Cao, H., Zi, Y., He, W., He, Z.: An improved time-varying mesh stiffness algorithm and dynamic modeling of gear-rotor system with tooth root crack. Eng. Fail. Anal. **42**, 157–177 (2014)